RSC Advances

REVIEW

View Article Online
View Journal | View Issue

Cite this: *RSC Adv.*, 2026, **16**, 7628

A systematic review on competitive screening and independent variable unification focused on PAA structural parameter calculation formulas in mild anodization

Chao Feng,[a] Shuang Li,[b] Yan Zhao[a] and Tianrui Zhai *[a]

Received 29th November 2025
Accepted 11th January 2026

DOI: 10.1039/d5ra09220e

rsc.li/rsc-advances

Porous anodized aluminium oxide (PAA) has wide and important applications in photonic crystals, energy science, nanotemplates, life science, medicine, aerospace and other scientific research and industrial manufacturing fields. The decisive factors determining its application value and specific performance are its own structural parameters. Therefore, the accurate calculation (but not destructive measurement) of each PAA structural parameter is of great significance for the design and application of PAA structures to satisfy different practical requirements. However, there is a significant problem because multiple distinct formulas proposed by different researchers are used for calculating single independent PAA structural parameters such as the pore diameter. Furthermore, these multiple distinct formulas for determining a single PAA structural parameter frequently yield different results. Compounding this issue, these single structural parameters serve as independent variables in formulas for calculating other PAA parameters. This propagation of uncertainty leads to multiple distinct results for other subsequent parameters. Consequently, in practice, for the calculation of a PAA structural parameter, it is difficult to discern which calculations are the most accurate. Regarding the aforementioned issues, this paper systematically reviews the key structural parameters of PAA and the most commonly used distinct calculation formulas of each key structural parameter. The independent variables of almost all mentioned calculation formulas are unified to the anodization voltage. Subsequently, extensive experimental data published by other researchers are substituted into all the formulas with the unified independent variable to perform an objective competitive screening for the optimal calculation formula of each PAA structural parameter. Finally, on the basis of the competitive screening and independent variable unification, an equation set of PAA structural parameter calculations is proposed for the accurate and convenient calculation of all key PAA structural parameters. The proposal of an equation set for the PAA structural parameter calculation provides a systematic, comprehensive theoretical model and mathematical tool for the design and calculation of PAA structures according to practical requirements in scientific research and engineering applications.

1 Introduction

Nanotechnology is currently one of the most researched fields of science. By some estimates, it promises to far exceed the impact of the industrial revolution. Nanotechnology provides materials like zero-dimensional nanodots,[1] one-dimensional nanowires,[2] two-dimensional nanoplanes of monatomic layer,[3] three-dimensional nanoframes,[4] periodical nanoarrays,[5] and nanocomposites,[6] which possess unique properties in comparison to macroscopic materials. These nanomaterials may be made from elemental carbon,[7] polymers,[8] metals,[9] oxides,[10] semiconductors,[11] and superconductors,[12] with potential applications in various fields of science like energy,[13] electronics,[14] information,[15] biology,[16] medicine,[17] environment,[18] catalysis,[19] food,[20] agriculture,[21] military[22] and many others. One of the most common nanotechnology issues is to obtain well-ordered arrays of nanostructures on a large scale with completely controllable structural parameters. Well-ordered arrays of nanostructures can be achieved by the application of various lithographic techniques such as electron beam lithography,[23] X-ray lithography,[24] and focused ion beam etching,[25] but these techniques have two major disadvantages: a limited working area of up to a few square mm and the high cost of manufacturing.[26,27] Therefore, some low-cost and controllable nanofabrication methods are more popular among researchers in nanoscience.

PAA membranes not only serve as well-ordered porous nanostructures but also as multifunctional templates for

---

[a] *School of Physics and Optoelectronic Engineering, Beijing University of Technology, 100 Pingleyuan, Chaoyang District, Beijing 100124, People's Republic of China. E-mail: trzhai@bjut.edu.cn*

[b] *School of Mathematics, Statistics and Mechanics, Beijing University of Technology, 100 Pingleyuan, Chaoyang District, Beijing 100124, People's Republic of China*

forming other nanostructures, effectively satisfying the demand for both porous nanomaterials and ordered templates. In particular, PAA membranes present many desirable properties such as tunable pore dimensions and membrane thicknesses,[28] good mechanical and thermal stabilities,[29] remarkable hardness,[30] low-cost preparation process,[31] and large area fabrication.[32] In recent decades, PAA membranes have attracted increasing interest because of their potential applications in ultrafiltration and gas separation,[33,34] hemodialysis,[35] nanofluids,[36] and Li rechargeable batteries.[37] Furthermore, PAA membranes are widely used as templates for the fabrication of nanomaterials.[38] Various sophisticated materials are deposited into the pores of PAA membranes by numerous techniques like electrochemical deposition,[39] chemical vapor deposition,[40] atomic layer deposition,[41] pulse laser deposition,[42] sol–gel technique,[43] molecular beam epitaxy,[44] and magnetron sputtering.[45] The nanostructures that are fabricated by filling the pores of PAA templates have uniform and adjustable diameter and length, and they can be obtained reproducibly and economically.

Well-ordered PAA membranes can be grown on the surface of aluminum by electrochemical oxidation,[46] which is referred to as anodization in acid electrolytes. The surface of a PAA membrane is a 2-dimensional closely packed hexagonal array shaped as a honeycomb with an open cylindrical channel pore in the center of each hexagonal unit.[47] The interior of a PAA membrane is characterized by parallel, non-interconnecting cylindrical channels extending from the surface down to the bottom of a PAA, and the channel bottoms are closed by a thin alumina barrier layer, as shown in Fig. 1(a). The key structural parameters of a PAA membrane include the interpore distance (D_i),[48] pore diameter (D_p),[49] pore wall thickness (T_w),[50] barrier layer thickness (T_b),[51] pore channel length (L_p) which is also known as porous layer thickness (T_p),[52] oxide layer thickness (T_o),[53] pore density (ρ),[54] and porosity (σ).[55] D_i, D_p, T_w, T_b, L_p, T_p and T_o are natural structural parameters, which can be measured and marked on a PAA directly, as shown in Fig. 1(a) and (c). ρ and σ are artificially defined structural parameters, which cannot be measured and marked on a PAA directly, and need to be calculated from the natural structural parameters. Every structural parameter is closely related to the capabilities of a PAA in various applications. For example, when a PAA is used for filtration, D_p will affect its filtration capability for particles with different sizes, and ρ will influence its filtration efficiency in a unit time. If a PAA is used as a template to assist the growth of various nanomaterials, L_p will directly determine the morphological characteristics of the final materials, which are nanodots, nanorods or nanowires. Thus, the accurate calculations for the PAA structural parameters are very important for the design and application of PAA structures. Depending on the accurate calculations, a PAA not only can be preliminarily designed to be the target structure according to the practical requirement before preparation but also can be directly applied after preparation without structural parameter measurements that would otherwise destroy or pollute the PAA membranes.

This paper summarizes various calculation formulas for each PAA structural parameter. To ensure objectivity and accuracy, this paper tests and contrasts the calculation result difference for each formula by the method of the mean square error (MSE) according to the experimental data of references, which have been published by other researchers. Based on a series of competitive screening, the optimal calculation formula of each PAA structural parameter is identified. All of the optimal calculation formulas are organized in the equation set of the PAA structural parameter calculation with a unified independent variable. The proposal of the equation set for the PAA structural parameter calculation will provide a comprehensive, systematic and accurate theoretical model and mathematical tool for predicting, designing and realizing PAA structural parameters to meet specific demands in practical applications.

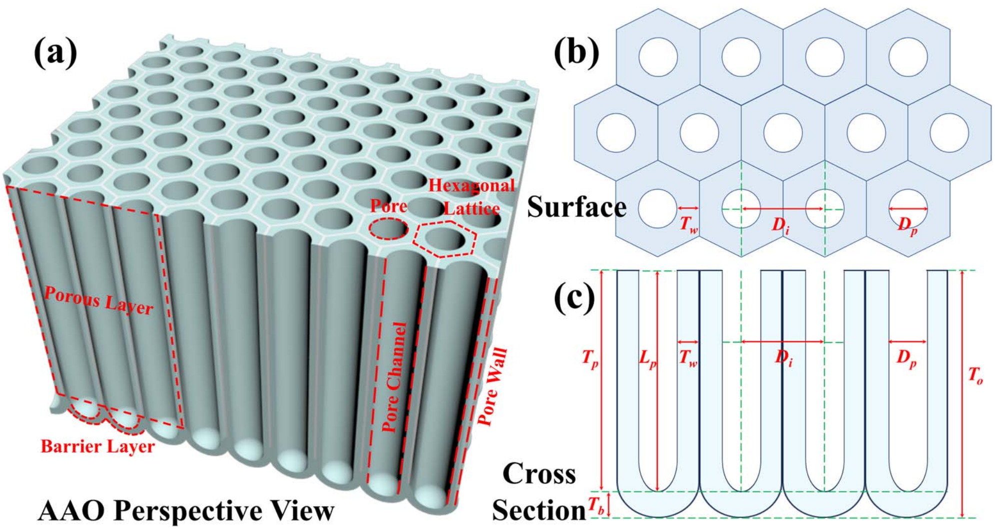

Fig. 1 The schematics of a PAA structure and the marking of the PAA structural parameters: (a) perspective view, (b) top view, (c) cross-sectional view.

2 Interpore distance (D_i)

D_i is the first natural structural parameter of a PAA. It is one of the two most important structural parameters, which directly or indirectly influences many other structural parameters. D_i limits the maximum value of D_p and directly determines ρ, and is one of the determining factors of T_w and σ. It is well known that D_i increases with increasing anodization voltage (U). Research groups have proposed different opinions to calculate D_i in relation to U. Leszek *et al.* proposed a 2.5 nm V^{-1} proportional relationship between D_i and U, as shown in formula (1):[56]

$$D_i = 2.5U \tag{1}$$

Thompson *et al.* proposed a 2.77 nm V^{-1} proportional constant for the dependence of D_i on U, as shown in formula (2):[57]

$$D_i = 2.77U \tag{2}$$

Hélio *et al.* proposed a 2.8-times proportional relationship between D_i and U, as shown in formula (3):[58]

$$D_i = 2.8U \tag{3}$$

Sun-Kyu *et al.* proposed a D_i calculation formula that is suitable for oxalic acid anodization, as shown in eqn (4):[59]

$$D_i = 2.75U - 5.2 \ \langle \text{oxalic} \rangle \tag{4}$$

Ebihara *et al.* proposed another D_i piecewise calculation formula suitable for oxalic acid anodization, which contains two different formulas corresponding to two different voltage intervals, as shown in formula (5):[60]

$$D_i = \begin{cases} 2.00U + 14.5 & (U \leq 20\ \text{V}) \\ 2.81U - 1.70 & (U \geq 20\ \text{V}) \end{cases} \quad \langle \text{oxalic} \rangle \tag{5}$$

Furthermore, there is a D_i calculation formula that is suitable for sulfuric acid anodization, as shown in eqn (6):[61]

$$D_i = 1.99U + 12.1 \ \langle \text{sulfuric} \rangle \tag{6}$$

Eqn (1)–(6) are all formulas that can be used to calculate D_i with the same independent variable U, but possess different mathematical expressions. Consequently, their calculation results differ from one another. In that case, which formula is the most accurate one? How does one choose and apply the D_i calculation formulas presented above? These are questions that must be addressed in practical applications. In order to clarify the above questions, extensive experimental (U, D_i) data published by other researchers (but not the authors of this paper) are substituted into formulas (1)–(6) to objectively test and compare the accuracy of formulas (1)–(6). Then, the MSE between each D_i formula calculation results and the corresponding experimental measurement D_i data is calculated using the MSE formula, as shown in eqn (7):

$$\text{MSE} = \frac{1}{n}\sum_{i=1}^{n}(y_i - \hat{y}_i)^2 \tag{7}$$

where MSE is the mean square error, y_i is the i-th experimental measurement value, $\hat{y}_i$ is the i-th calculation result, and n is the number of research samples. A smaller MSE between the experimental measurement values and the calculation results indicate a more accurate formula.

Table S1 presents the experimental measurement data of D_i and the corresponding U from different ref. 27, 56 and 62–72. The (U, D_i) data point from the Table S1 is plotted as the black dots shown in Fig. 2(a). In this figure, the linear regressions of formulas (1)–(6) are shown as the red, orange, yellow, green, cyan and blue curve, respectively. In Fig. 2(a), visually, the linear regression of formula (1) appears to agree better for the experimental data than the other formulas when the anodization voltages are higher than 80 V. However, the differences between the experimental data and the linear regressions of formulas (1)–(6) are less clear and not easily discernible at voltages below 80 V. In order to quantitatively evaluate the errors between the experimental data and the calculation results from formulas (1)–(6), the U data from Table S1 were substituted into formulas (1)–(6), and the MSE between the results of each formula and the corresponding experimental measurement D_i data were calculated.

All the data from Table S1 were respectively substituted in formulas (1)–(6). The MSE values of the six formulas are shown in Fig. 2(b) and the 'universal' row of Table 1. Taken together, these results demonstrate that formula (1) is the best equation as the universal D_i calculation formula because it has the smallest MSE among formulas (1)–(6), when the electrolyte type is not specially considered. When all the oxalic acid anodization data from Table S1 are substituted into formulas (1)–(6), the resulting MSE values of the six formulas shown in Fig. 2(c) and the 'oxalic' row of Table 1 indicate that formula (1) is the best D_i calculation equation for oxalic acid anodization if the electrolyte is specified as only oxalic acid. When all the sulfuric acid anodization data of Table S1 are substituted into formulas (1)–(6), the MSE values of the six formulas shown in Fig. 2(d) and the 'sulfuric' row of Table 1 demonstrate that formula (6) is the best D_i calculation equation for sulfuric acid anodization if the electrolyte is specified as only sulfuric acid. In the event that all the phosphoric acid anodization data of Table S1 are substituted into formulas (1)–(6), the MSE values of the six formulas shown in Fig. 2(e) and the 'phosphoric' row of Table 1 display that formula (1) is the best D_i calculation equation for phosphoric acid anodization if the electrolyte is specified as only phosphoric acid. In the event that all the inorganic acid anodization data of Table S1 are substituted into formulas (1)–(6), the MSE values of the six formulas shown in Fig. 2(f) and the 'inorganic' row of Table 1 show that formula (1) is the best D_i calculation equation that is suitable for inorganic acid anodization when the electrolyte is various inorganic acids. In the event that all the organic acid anodization data of Table S1 are substituted into formulas (1)–(6), the MSE values for the six formulas shown in Fig. 2(g) and the 'organic' row of Table 1 reveal that formula (1) is the best D_i calculation equation that is

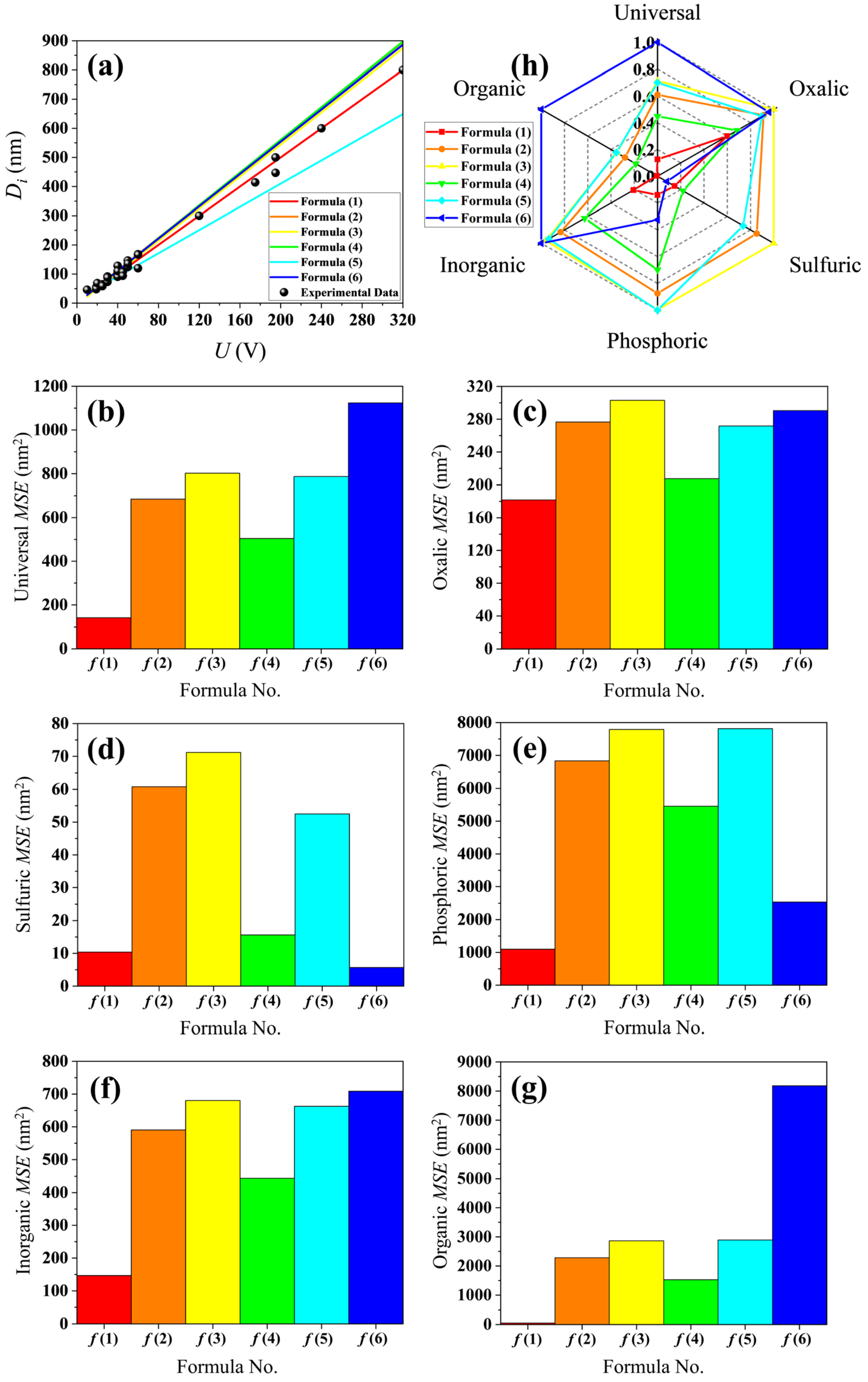

Fig. 2 Contrastive research between the calculation results of formulas (1)–(6) and the experimental data. (a) Experimental data dots of Table S1 and the linear regression of formulas (1)–(6). (b) Histogram of MSE when the electrolyte type is not specified. (c) Histogram of MSE when the electrolyte is specified as only oxalic acid. (d) Histogram of MSE when the electrolyte is specified as only sulfuric acid. (e) Histogram of MSE when the electrolyte is specified as only phosphoric acid. (f) Histogram of MSE when the electrolyte is specified as inorganic acid. (g) Histogram of MSE when the electrolyte is specified as an organic acid. (h) Normalized radar plot for MSE of formulas (1)–(6) in universal and oxalic, sulfuric, phosphoric, inorganic, organic acid anodization.

Table 1 MSE of the calculation results from formulas (1)–(6) against the experimental measurement D_i data of Table S1

	Mean squared error					
Electrolyte type	f (1)	f (2)	f (3)	f (4)	f (5)	f (6)
Universal	**141.6**	684.6	801.8	504.0	786.8	1124.1
Oxalic	**181.7**	276.6	303.1	207.5	271.9	290.6
Sulfuric	10.4	60.8	71.2	15.6	52.5	**5.7**
Phosphoric	**1096.3**	6841.2	7788.5	5457.3	7817.1	2536.6
Inorganic	**146.8**	590.4	680.5	443.8	662.8	708.9
Organic	**52.1**	2286.9	2865.3	1527.4	2894.9	8182.3

suitable for organic acid anodization when the electrolyte is various organic acids. Fig. 2(h) is the normalized radar plot of the MSE values for formulas (1)–(6) in universal and oxalic, sulfuric, phosphoric, inorganic, organic acid anodization, respectively. This visualization allows for an easy comparison on the competitive rankings on MSE values from formulas (1)–(6). For example, along the inorganic axis, the normalized MSE values indicate the following accuracy ranking of inorganic acid anodization from best to worst: formula (1) (red curve) > formula (4) (green curve) > formula (2) (orange curve) > formula (5) (cyan curve) > formula (3) (yellow curve) > formula (6) (blue curve). Beyond analyzing the individual axes, the total area enclosed by each curve on the radar plot provides a measure of a formula's overall universality. Formula (1) with the smallest area (red curve) is the most universally accurate across all electrolyte types. This method is different from the above method, according to the direction and normalized MSE value to estimate, but it obtains the same conclusion.

Section summary: According to a series of competitive screening based on numerous experimental data from various references, the existing optimal D_i calculation formulas are verified as follows:

$$D_i = 2.5U \langle \text{universal} \rangle \qquad (1)$$

$$D_i = 2.5U \langle \text{oxalic} \rangle \qquad (1)$$

$$D_i = 1.99U + 12.1 \langle \text{sulfuric} \rangle \qquad (6)$$

$$D_i = 2.5U \langle \text{phosphoric} \rangle \qquad (1)$$

$$D_i = 2.5U \langle \text{inorganic} \rangle \qquad (1)$$

$$D_i = 2.5U \langle \text{organic} \rangle \qquad (1)$$

Eqn (1) is the optimal D_i calculation formula in almost all cases. The only exception occurs when sulfuric acid is specified as the only electrolyte, with eqn (6) performing slightly better than eqn (1), albeit by a small margin.

3 Pore diameter (D_p)

D_p is the second natural structural parameter of a PAA, and one of the two most important PAA structural parameters. The nanoscale-size, self-organized, well-ordered nanopores of a PAA are adjustable objectively.[28] This property makes the PAA membranes become one of the most popular templates for the growth of nanodots,[73] nanorods,[74] nanopillars,[75] nanowires,[76] and nanotubes,[77] which exhibit special performances such as ferroelectric multi-domains,[73] SERS,[74] anti-biofilm,[75] photocatalysis,[76] and wave absorption.[77]

For a PAA, the maximum D_p value is limited by D_i, but the born value of D_p is not directly determined by D_i. Specifically, there are two kinds of D_p values for describing the size of PAA nanopores: the born value of D_p ($D_{\text{p-born}}$) and the pore-widening value of D_p ($D_{\text{p-widening}}$). $D_{\text{p-born}}$ is determined by the anodization voltage during PAA fabrication. It is the initial D_p value after PAA anodization without pore-widening treatments. $D_{\text{p-widening}}$ is the D_p value after pore-widening treatments on the foundation of $D_{\text{p-born}}$. It is a post-processing parameter, but not an original parameter. After anodization is complete, the $D_{\text{p-widening}}$ can be easily and irreversibly adjusted to be any value from the $D_{\text{p-born}}$ to the maximum (D_i) by pore-widening treatments. It should be emphasized that in this paper, all of the mentioned D_p refer to $D_{\text{p-born}}$, but not $D_{\text{p-widening}}$.

It is generally considered that the anodization voltage has the most dramatic effect on D_p. D_p increases as the anodization voltage increases. Some research suggests that PAA nanopore formation is accompanied by volume expansion at the metal–oxide interface. This volume expansion is given by the Pilling–Bedworth ratio (PBR), which is expressed as eqn (8):[78]

$$\text{PBR} = \frac{\text{Volume of oxide produced}}{\text{Volume of metal consumed}} \qquad (8)$$

Due to volume expansion, the oxide is pushed in tangential and upward directions, moving the oxide walls upward, thereby increasing the height of the pore wall. A higher voltage is associated with a higher current density, which leads to a higher volume expansion, resulting in more oxide being pushed in both tangential and upward directions. Consequently, PAA pore walls will be squeezed more by the higher voltage, thereby achieving a larger D_p.

Due to the powerful influence of voltage on D_p, many research groups have proposed their own D_p calculation formulas in different mathematic expressions with U as the independent variable. Leszek *et al.* reported a proportionality constant of 0.9 nm V^{-1} between D_p and U, and the corresponding formula is shown in eqn (9):[56]

$$D_p = 0.9U \qquad (9)$$

O'Sullivan and Wood presented a relationship between D_p and U with a correlation constant of 1.29 nm V^{-1}, as given in formula (10):[79]

$$D_p = 1.29U \qquad (10)$$

Palibroda *et al.* reported the dependence of the PAA pore diameter on the anodization voltage, as given in formula (11):[80]

$$D_p = 0.709U + 4.986 \qquad (11)$$

In contrast to the above three linear formulas (9)–(11), Alaa *et al.* proposed a nonlinear D_p calculation formula, as given in eqn (12):[81]

$$D_p = 14\,e^{0.02U} \tag{12}$$

Faced with the various D_p calculation formulas with different mathematical expressions, the method for confirming the optimal D_p calculation formula is the same as the competitive screening described above for the optimal D_i calculation formula. Extensive experimental (U, D_p) data published by other researchers were substituted into formulas (9)–(12) to objectively test and contrast their accuracy. Then, the MSE values between each D_p formula calculation result and the corresponding experimental measurement D_p data are calculated. A smaller MSE between the experimental measurement values and calculation results indicates that the formula is more accurate.

Table S2 lists the experimental measurement data of D_p and the corresponding U from different ref. 27, 56, 62, 65–68, 70, 78 and 82–89. The (U, D_p) data points of Table S2 are shown as the black dots in Fig. 3(a), while the regression lines of formulas (9)–(12) are shown as the red, orange, green and blue curves, respectively. In Fig. 3(a), visually, the regression line of formula (11) is in better agreement with the experimental data than the other formulas when the anodization voltages are higher than 80 V. However,

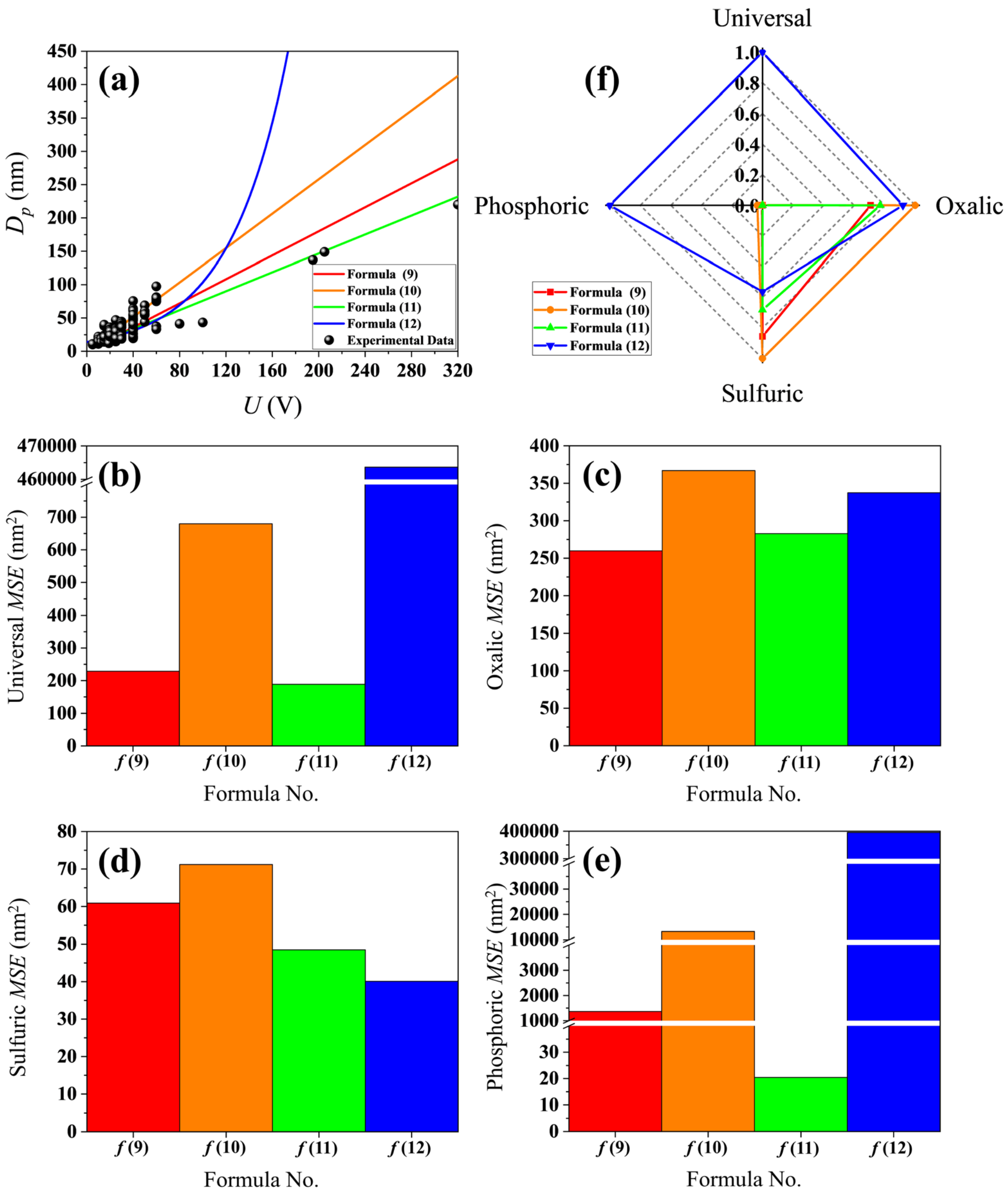

Fig. 3 Contrastive research between the calculation results of formulas (9)–(12) and the experimental data. (a) Experimental data dots of Table S2 and linear regression of formulas (9)–(12). (b) Histogram of MSE when the electrolyte type is not specified. (c) Histogram of MSE when the electrolyte is specified as only oxalic acid. (d) Histogram of MSE when the electrolyte is specified as only sulfuric acid. (e) Histogram of MSE when the electrolyte is specified as only phosphoric acid. (f) Normalized radar plot for MSE of formulas (9)–(12) in universal and oxalic, sulfuric, phosphoric acid anodization.

when the anodization voltages are lower than 80 V, the contrast between the experimental data and regression line of formulas (9)–(12) is not clear and not visually observed. In order to separately quantify the errors between the experimental data and the calculation results of formulas (9)–(12), the U data of Table S2 are substituted into formulas (9)–(12), and the MSE values between the results of each formula and the corresponding experimental measurement D_p data are then calculated.

In the event that all the data of Table S2 are respectively substituted in formulas (9)–(12), the MSE values of the four formulas shown in Fig. 3(b) and the 'universal' row of Table 2 demonstrate that formula (11) is the best equation as the universal D_p calculation formula because of its smallest MSE among formulas (9)–(12), when the electrolyte kind is not specially considered. In the event that all the oxalic acid anodization data of Table S2 are substituted into formulas (9)–(12), the MSE values of the four formulas shown in Fig. 3(c) and the 'oxalic' row of Table 2 indicate that formula (9) is the best D_p calculation equation for oxalic acid anodization because of its smallest MSE, if the electrolyte is specified as only oxalic acid. In the event that all the sulfuric acid anodization data of Table S2 are substituted into formulas (9)–(12), the MSE values of the four formulas shown in Fig. 3(d) and the 'sulfuric' row of Table 2 indicate that formula (12) is the best D_p calculation equation for sulfuric acid anodization because of its smallest MSE if the electrolyte is specified as only sulfuric acid. In the event that all the phosphoric acid anodization data of Table S2 are substituted into formulas (9)–(12), the MSE values of the four formulas shown in Fig. 3(e) and the 'phosphoric' row of Table 2 show that formula (11) is the best D_p calculation equation for phosphoric acid anodization because of its smallest MSE if the electrolyte is specified as only phosphoric acid. Fig. 3(f) is the normalized radar plot for the MSE values of formulas (9)–(12) in universal and oxalic, sulfuric, phosphoric acid anodization. It exhibits the competitive ranking for the MSE values of formulas (9)–(12) in different electrolyte anodizations at a glance. The green closed curve surrounds the smallest area, which also indicates that formula (11) is the best equation for the universal calculation of D_p from a holistic view. The area method is different from the method of estimating based on the direction and MSE value of each axis, yet both approaches lead to the same conclusion.

It should be emphasized that the existing mainstream D_p calculation formulas are primarily expressed as single-variable functions of U, but voltage is not the sole factor influencing D_p. From the perspective of anodization conditions, besides voltage, many other factors can influence D_p to different extents, such as the anodization temperature, electrolyte concentration and electrolyte type.[83] By focusing exclusively on voltage but ignoring other factors, the existing D_p formulas inevitably introduce errors, the extent of which varies across different complex anodization conditions. For example, the D_p distribution is notably broad at lower voltages in Fig. 3(a). The reason lies not in the lower voltage itself, but in the inherent limitation of the existing D_p formulas, which rely on voltage as their sole independent variable. The solution lies in systematically conducting a quantitative investigation into more influence factors on D_p, such as the anodization temperature, electrolyte concentration, electrolyte type and anodization duration, rather than focusing only on the voltage. Then, a new D_p calculation formula can be proposed with multiple independent variables that incorporate all key influencing factors, to replace all existing formulas that rely solely on voltage. The aforementioned issue exists not only in the D_p calculation formula, but more broadly in both the already-discussed D_i and the various structural parameters to be discussed in subsequent chapters. This currently remains a significant research gap and a crucial research topic for future studies.

Table 2 MSE of the calculation results from formulas (9)–(12) against the experimental measurement D_p data of Table S2

	Mean squared error			
Electrolyte type	f (9)	f (10)	f (11)	f (12)
Universal	228.8	679.7	**189.02**	463 669.0
Oxalic	**259.7**	367.1	282.8	337.3
Sulfuric	60.9	71.2	48.5	**40.1**
Phosphoric	1371.3	13 225.2	**20.4**	395 853.4

In addition, it is well known that the growth of PAA pores is a multi-mechanism process. The size of D_p is determined by the combined effect of pore growth and acid electrolyte corrosion acting simultaneously. Unfortunately, none of the existing D_p calculation formulas are derived from a separate, quantitative study of the pore growth mechanism and the acid electrolyte corrosion mechanism. Therefore, none of the existing formulas can be used to independently explain the impact of either the pore growth mechanism or the acid electrolyte corrosion effect on D_p. Any existing D_p calculation formula serves to calculate the aggregate result arising from all factors that influence D_p. Separating and quantitatively studying the individual effects of the pore growth mechanism and the acid electrolyte corrosion on D_p remains an outstanding research gap at present and a crucial research topic for future studies.

Section summary: according to a series of competitive screening based on numerous experimental data from other references, the existing optimal D_p calculation formulas are verified as follows:

$$D_p = 0.709U + 4.986 \langle \text{universal} \rangle \tag{11}$$

$$D_p = 0.9U \langle \text{oxalic} \rangle \tag{9}$$

$$D_p = 14\,e^{0.02U} \langle \text{sulfuric} \rangle \tag{12}$$

$$D_p = 0.709U + 4.986 \langle \text{phosphoric} \rangle \tag{11}$$

Eqn (11) is the universal D_p calculation formula for common cases. In the case of one of the two exceptions, when oxalic acid is specified as the only electrolyte, eqn (9) is slightly better than eqn (11) with a small advantage. For the other exception, when sulfuric acid is specified as the only electrolyte, eqn (12) is slight better than eqn (11) with a small advantage.

4 Pore wall thickness (T_w)

Pore wall thickness is the third natural structural parameter of a PAA. It affects the mechanical strength of PAA membranes. A thicker pore wall thickness is indicative of a more robust and free-standing PAA membrane. It is widely recognized that in the perfect hexagonal arrangement of pores, T_w can be calculated by formula (13):[90]

$$T_w = \frac{D_i - D_p}{2} \tag{13}$$

where D_i is the interpore distance with the unit of nm, and D_p is the (born) pore diameter with the unit of nm. In formula (13), there are two independent variables, D_i and D_p. According to the above discussions about D_i and D_p, both D_i and D_p are functions of U. Thus, T_w also can be derived to be a function of U. Therefore, if substituting the above optimal D_i and D_p calculation formulas into formula (13), the optimal T_w calculation formulas as a function of U can be obtained.

After substituting the universal D_i calculation formula (1) and the universal D_p calculation formula (11) into formula (13), the universal T_w calculation formula is obtained, as shown in eqn (14):

$$T_w = 0.8955U - 2.493 \langle \text{universal} \rangle \tag{14}$$

After substituting oxalic D_i calculation formula (1) and oxalic D_p calculation formula (9) into (13), the optimal T_w calculation formula specific to oxalic acid anodization is obtained, as shown in eqn (15):

$$T_w = 0.8U \langle \text{oxalic} \rangle \tag{15}$$

After substituting sulfuric D_i calculation formula (6) and sulfuric D_p calculation formula (12) into (13), the optimal T_w calculation formula specific to sulfuric acid anodization is obtained, as shown in eqn (16):

$$T_w = 0.995U - 7\,e^{0.02U} + 6.05 \langle \text{sulfuric} \rangle \tag{16}$$

Based on derivations, the optimal T_w calculation formulas specific to phosphoric acid anodization are the same as the universal formula (14).

Section summary: according to a series of derivations, the existing optimal T_w calculation formula with U as the only independent variable is shown as follows:

$$T_w = 0.8955U - 2.493 \langle \text{universal} \rangle \quad (14)$$

$$T_w = 0.8U \langle \text{oxalic} \rangle \quad (15)$$

$$T_w = 0.995U - 7\,e^{0.02U} + 6.05 \langle \text{sulfuric} \rangle \quad (16)$$

$$T_w = 0.8955U - 2.493 \langle \text{phosphoric} \rangle \quad (14)$$

Depending on the above optimal T_w calculation formulas for different electrolytes, the T_w of a PAA can be calculated directly from U, rather than first calculating D_i and D_p separately.

5 Barrier layer thickness (T_b)

Applications of PAA structures are limited sometimes, such as when using PAA nanochannels as templates to grow nanowires by electrochemical deposition. As reported, in a system of electrochemical deposition, one of the most critical limitations is the non-conductive property of the PAA barrier layer. The high electrical resistance generated by the barrier layer isolates the metallic base from the electrochemical deposition bath. In other words, an electrochemical contact would be necessary for electrochemical deposition inside the PAA pores. For reasons similar to the above mentioned, barrier layer removal is very important for actual PAA applications in some special fields. Hence, in order to remove a barrier layer accurately with as little damage as possible to the PAA nanochannel structure, the T_b value of a PAA needs be predicted and calculated precisely in practice.

T_b is the fourth natural structural parameter of a PAA. Digby described PAA barrier layer growth using the point defect model.[91] Based on this model, oxygen ion vacancies diffuse from the oxide–metal interface to solution–oxide interface. In contrast, aluminum ion vacancies diffuse from the solution–oxide interface to oxide–metal interface. The key contribution to the PAA barrier layer growth is supplied by the oxygen anion. It is demonstrated that about 60% of T_b is formed at the oxide–metal interface by migration of O^{2-} and OH^- ions inwards, and the remaining 40% of T_b is formed at the solution–oxide interface by migration of Al^{3+} ions outwards.[92]

It is well documented that T_b is proportional to U. However, different researchers have proposed different values for the proportionality coefficient between T_b and U. Lee and Park reported that T_b increases with U, as shown in formula (17):[93]

$$T_b = U \tag{17}$$

Thompson *et al.* proposed a 1.05 nm V^{-1} ratio relationship between T_b and U, as shown in formula (18):[57]

$$T_b = 1.05U \tag{18}$$

Kjyohito *et al.* gave a 1.1 nm V^{-1} proportionality coefficient between T_b and U, as shown in formula (19):[94]

$$T_b = 1.1U \tag{19}$$

Sachiko *et al.* defined a 1.14 nm V^{-1} ratio between T_b and U, as shown in formula (20):[95]

$$T_b = 1.14U \tag{20}$$

Sousa *et al.* presented a 1.3 nm V^{-1} phenomenological constant between T_b and U, as shown in formula (21):[96]

$$T_b = 1.3U \tag{21}$$

Dmitri *et al.* claimed the anodizing ratio of 1.4 nm V^{-1} to determine T_b by U, as shown in formula (22):[97]

$$T_b = 1.4U \tag{22}$$

In addition to the linear relationship between T_b and U, T_w and D_i have also been reported as the independent variables that are needed to calculate T_b. In the opinion of Ebihara *et al.*, T_b formed during oxalic or sulfuric acid anodization is different and can be calculated by T_w, as respectively shown in formulas (23) and (24):[56]

$$T_b = 1.12 \times T_w \langle \text{oxalic} \rangle \tag{23}$$

$$T_b = 1.33 \times T_w \langle \text{sulfuric} \rangle \tag{24}$$

where T_w is the pore wall thickness with the unit of nm. Nielsch *et al.* suggested that T_b is proportional to D_i, as shown in formula (25):[98]

$$T_b \cong \frac{D_i}{2} \tag{25}$$

where D_i is the interpore distance with the unit of nm.

Apparently, the T_b calculation formulas of eqn (17)–(25) have different independent variables: U is the independent variable of formulas (17)–(22), T_w is the independent variable of formulas (23) and (24), and D_i is the independent variable of formula (25). It is difficult to directly contrast the accuracies of all the formulas. However, formulas (23)–(25) can be reformulated to use U as their independent variables. This is possible because both T_w and D_i are functions of U in essence, according to the previous discussions. Thus, when the oxalic T_w calculation formula (15) is substituted into formula (23), a new T_b calculation formula with U as its independent variable suitable for oxalic acid anodization is obtained, as shown in eqn (26):

$$T_b = 0.896U \langle \text{oxalic} \rangle \tag{26}$$

Substituting the sulfuric T_w calculation formula (16) into (24) yields a new T_b calculation formula with U as its independent variable suitable for sulfuric acid anodization, as shown in eqn (27):

$$T_b = 1.32335U - 9.31\,e^{0.02U} + 8.0465 \langle \text{sulfuric} \rangle \tag{27}$$

When the universal D_i calculation formula (1) is substituted into formula (25), a new universal T_b calculation formula with U as its independent variable is obtained, as shown in eqn (28):

$$T_b = 1.25U \langle \text{universal} \rangle \tag{28}$$

Substituting the sulfuric D_i calculation formula (6) into (25) yields a new T_b calculation formula with U as its independent variable specific to sulfuric acid anodization, as shown in eqn (29):

$$T_b = 0.995U + 6.05 \langle \text{sulfuric} \rangle \tag{29}$$

After all the independent variables of formulas (23)–(25) are unified by U to obtain formulas (26)–(29), all the new formulas have the same independent variable as formulas (17)–(22). Thus, the accuracy of formulas (17)–(22) and (26)–(29) can be tested and compared together. For competitively screening the optimal Tb calculation formula, numerous experimental (U, T_b) data published by other researchers are substituted into formulas (17)–(22) and (26)–(29). Then, the MSE values between each T_b formula calculation result and the corresponding experimental measurement T_b data are calculated to objectively test and contrast the accuracy of formulas (17)–(22) and (26)–(29). A smaller MSE value indicates that the formula is more accurate.

Table S3 presents experimental measurement data of T_b and the corresponding U from different ref. 56, 62, 93 and 99–104. The (U, T_b) data points of Table S3 are shown as the black dots in Fig. 4(a), and the regression lines of formulas (17)–(22) and (26)–(29) are shown as the black, pink, red, orange, yellow, green, olive, cyan, blue and violet curves, respectively. In order to separately quantify the errors between the experimental data and the calculation results of formulas (17)–(22) and (26)–(29), the U data of Table S3 are substituted into formulas (17)–(22) and (26)–(29). Then, the MSE between the result of each formula and the corresponding experimental measurement T_b data is calculated.

In the event that all the data of Table S3 are respectively substituted in formulas (17)–(22) and (26)–(29), the MSE values of the ten formulas shown in Fig. 4(b) and the 'universal' row of Table 3 demonstrate that formula (19) is the best equation as the universal T_b calculation formula due to its minimal MSE among formulas (17)–(22) and (26)–(29), when the electrolyte is not specially considered. In the event that all the oxalic acid anodization data of Table S3 are substituted into formulas (17)–(22) and (26)–(29), the MSE values of the ten formulas shown in Fig. 4(c) and the 'oxalic' row of Table 3 indicate that formula (19) is the best T_b calculation equation specific to oxalic acid anodization, if the electrolyte is specified as only oxalic acid. In the event that all the sulfuric acid anodization data of Table S3 are substituted into formulas (17)–(22) and (26)–(29), the MSE values of the ten formulas shown in Fig. 4(d) and the 'sulfuric' row of Table 3 exhibit that formula (19) is the best T_b calculation equation specific to sulfuric acid anodization, if the electrolyte is specified as only sulfuric acid. In the event that all the phosphoric acid anodization data of Table S3 are substituted into formulas (17)–(22) and (26)–(29), the MSE values of the ten formulas shown in Fig. 4(e) and the 'phosphoric' row of Table 3 show that formula (20) is the best T_b calculation equation specific to phosphoric acid anodization, if the electrolyte is specified as only phosphoric acid. Fig. 4(f) is the normalized radar plot for the MSE of formulas (17)–(22) and (26)–(29) in universal and oxalic, sulfuric and phosphoric acid anodization. It exhibits the competitive ranking for the MSE of (17)–(22) and (26)–(29) in different electrolyte anodization at a glance. Furthermore, the red closed curve surrounds the smallest area, which also indicates that formula (19) is the best equation for the universal calculation of T_b from a holistic view. This area-based evaluation method differs from the estimating performance based on the MSE value of each axis, yet both approaches lead to the same conclusion.

Section summary: according to a series of competitive screening based on numerous experimental data from various other references, the existing optimal T_b calculation formulas are verified as follows:

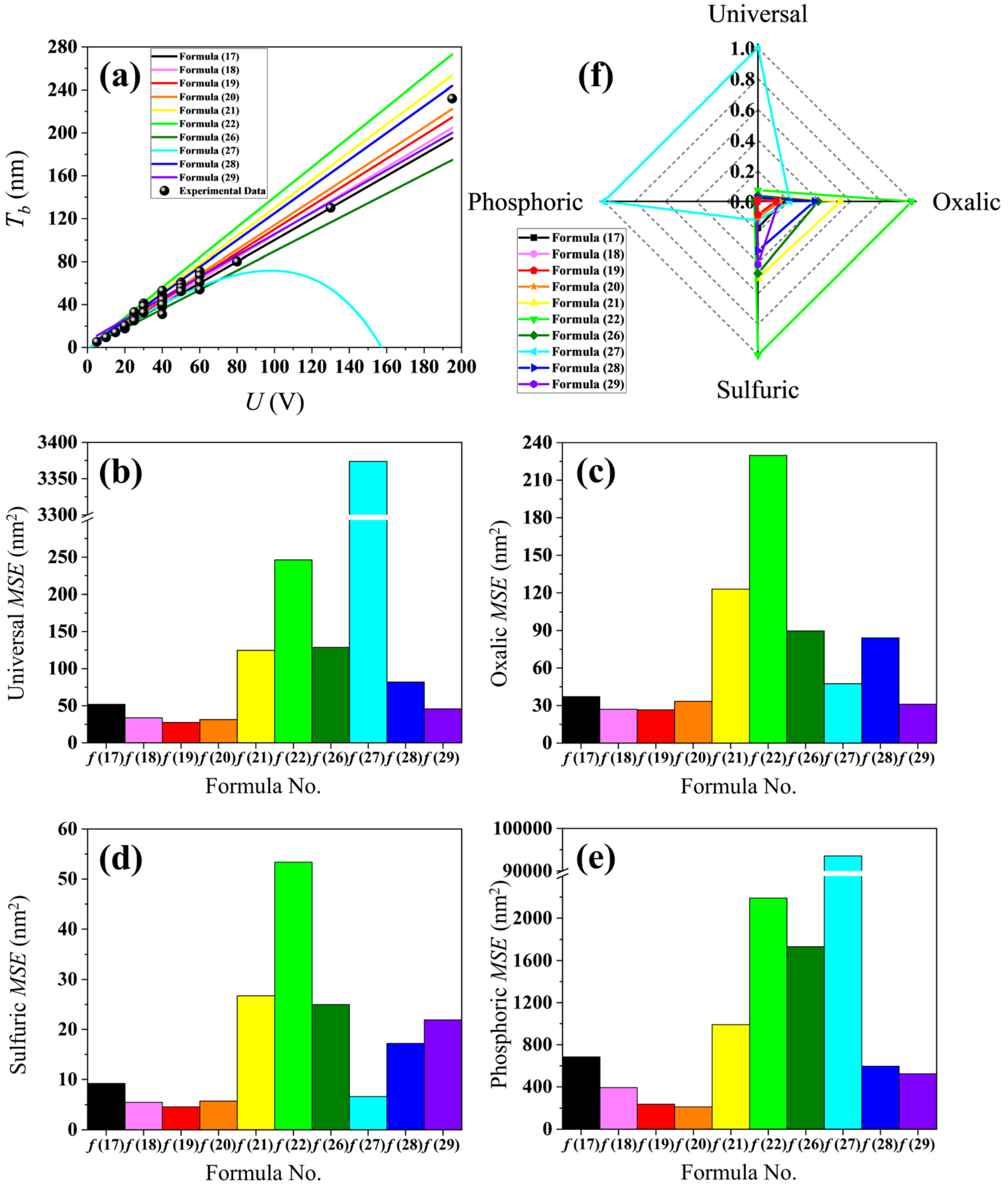

Fig. 4 Contrastive research between the calculation results of formulas (17)–(22) and (26)–(29) and the experimental data. (a) Experimental data dots of Table S3 and linear regression of formulas (17)–(22) and (26)–(29). (b) Histogram of MSE when the electrolyte type is not specified. (c) Histogram of MSE when the electrolyte is specified as only oxalic acid. (d) Histogram of MSE when the electrolyte is specified as only sulfuric acid. (e) Histogram of MSE when the electrolyte is specified as only phosphoric acid. (f) Normalized radar plot for MSE of formulas (17)–(22) and (26)–(29) in universal and oxalic, sulfuric and phosphoric acid anodization.

Table 3 MSE of the calculation results from formulas (17)–(22) and (26)–(29) against the experimental measurement T_b data of Table S3

	Mean squared error									
Electrolyte type	f (17)	f (18)	f (19)	f (20)	f (21)	f (22)	f (26)	f (27)	f (28)	f (29)
Universal	51.8	33.6	**27.5**	31.4	124.7	246.3	128.7	3373.8	82.1	45.9
Oxalic	37.2	27.1	**26.7**	33.4	122.9	229.8	89.7	47.5	84.2	31.1
Sulfuric	9.2	5.5	**4.6**	5.7	26.7	53.4	25.0	6.6	17.2	21.9
Phosphoric	684.5	392.4	237.6	**212.7**	991.6	2192	1731	93 533	597.1	524.2

$$T_\mathrm{b} = 1.1U\,\langle\text{universal}\rangle \tag{19}$$

$$T_\mathrm{b} = 1.1U\,\langle\text{oxalic}\rangle \tag{19}$$

$$T_\mathrm{b} = 1.1U\,\langle\text{sulfuric}\rangle \tag{19}$$

$$T_\mathrm{b} = 1.14U\,\langle\text{phosphoric}\rangle \tag{20}$$

Formula (19) is the optimal T_b calculation formula in almost all cases. The only exception is for phosphoric acid anodization, where formula (20) performs slightly better.

6 Pore channel length (L_p), also known as the porous layer thickness (T_p)

The pore channel length is the porous layer thickness of a PAA. Thus, L_p and T_p are the same structural parameter. They are both the fifth natural structural parameter of a PAA. L_p and T_p are closely related with practical applications of through-hole PAA. A through-hole PAA can be obtained by opening-hole process, which is typically carried out in a phosphoric acid solution.[93] During the opening-hole process, the barrier layer of a PAA membrane is immersed in a phosphoric acid solution and subjected to chemical etching until removed completely.

L_p and T_p are very important parameters for through-hole PAA applications in different fields. A thick T_p is an advantageous property for separation applications, because it helps to maintain the mechanical integrity of through-hole PAA filter membranes during processing, handling and filtering. This allows a through-hole PAA to tolerate a higher pressure-difference between two sides of a through-hole PAA filter membrane during the filtration process, thereby increasing the separation rate and efficiency. However, a short L_p and thin T_p are required when a through-hole PAA is used as a mask for sputtering deposition, because a L_p that is too long and a T_p that is too thick will prevent the deposited materials from smoothly reaching the target substrate. Therefore, accurate calculations for L_p and T_p of a PAA are very important for practical applications. Hwang *et al.* proposed that the L_p of a PAA is proportional to the anodization duration (D). The linear relationship can be formulated as eqn (30):[59]

$$L_\mathrm{p} = 125.53D - 147.75 \tag{30}$$

where L_p is the pore channel length of PAA and is equal to T_p in units of nm, and D is the anodization duration in units of min. They also emphasized that the linear relationship cannot be maintained when the anodization is carried out for an excessively long duration. The subsequent research demonstrates that the thickness of a PAA is not in a strictly linear relationship with the anodization duration. The appearance of a limiting thickness will be observed when an anodization duration is excessive. In fact, the thickness of a PAA membrane is usually less than 200 μm in most of the literature reports. For a PAA membrane prepared with a short or moderate duration, its pore channel length can be calculated by formula (30). However, for a PAA membrane prepared by an excessive anodization duration, formula (30) is not accurate. A longer duration indicates a bigger error.

Section summary: The L_p and T_p calculation formula for a short or moderate anodization duration is eqn (30):

$$L_\mathrm{p} = T_\mathrm{p} = 125.53D - 147.75 \tag{30}$$

where L_p is the pore channel length in units of nm, T_p is the porous layer thickness in units of nm, D is the anodization duration in units of min. However, formula (30) is not accurate for a PAA fabricated with an excessive anodization duration.

7 Oxide layer thickness (T_o)

T_o is the sixth natural structural parameter of a PAA. It is the total thickness of an integral PAA membrane and is, in fact, equal to the sum of T_b and T_p. Beyond traditional applications, research in the last decade has revealed that an intact PAA with a barrier layer can be used as nanofluidic devices by taking advantage of its ionic current rectification property, such as ultrasensitive capture,[105] detection,[106] and controlled release of drugs[107] have been demonstrated. The T_o calculation formula is given by eqn (31):

$$T_\mathrm{o} = T_\mathrm{b} + T_\mathrm{p} \tag{31}$$

where T_o is the oxide layer thickness in units of nm, T_b is the barrier layer thickness in units of nm, and T_p is the porous layer thickness in units of nm. Since T_b is the function of U, as shown as formulas (19) and (20), and T_p is the function of D, as shown as formula (30), formula (31) can be further derived to be a new T_o calculation formula with U and D as the independent variables. After substituting formulas (19) and (30) into (31), a new T_o calculation formula with anodization conditions as independent variables suitable for universal and oxalic, sulfuric acid anodization is obtained and expressed as eqn (32):

$$T_\mathrm{o} = 1.1U + 125.53D - 147.75 \tag{32}$$

After substituting formulas (20) and (30) into (31), the new T_o calculation formula with anodization conditions as independent variables suitable for phosphoric anodization is obtained and expressed as eqn (33):

$$T_\mathrm{o} = 1.14U + 125.53D - 147.75 \tag{33}$$

Section summary: according to a series of derivations, the T_o calculation formulas with anodization conditions as independent variables are as follows:

$$T_\mathrm{o} = 1.1U + 125.53D - 147.75\,\langle\text{universal}\rangle \tag{32}$$

$$T_\mathrm{o} = 1.1U + 125.53D - 147.75\,\langle\text{oxalic}\rangle \tag{32}$$

$$T_o = 1.1U + 125.53D - 147.75 \langle \text{sulfuric} \rangle \tag{32}$$

$$T_o = 1.14U + 125.53D - 147.75 \langle \text{phosphoric} \rangle \tag{33}$$

Eqn (32) is the optimal T_o calculation formula in almost all cases. The only exception is when phosphoric acid is specified as the only electrolyte; in this case, eqn (33) is slightly better than eqn (32).

8 Pore density (ρ)

ρ is the seventh PAA structural parameter, which is not a natural one but is artificially defined. For a well-ordered PAA with a standard hexagonal lattice, ρ is defined as the total number of pores on 1 cm^2 of surface area.[65] The formula of ρ is derived according to the definition of the pore density, given by eqn (34):[65]

$$\rho = \frac{2 \times 10^{14}}{\sqrt{3} \times {D_i}^2} \tag{34}$$

where ρ is the pore density in units of cm^{-2}, and D_i is the interpore distance in units of nm.

The derivation process of eqn (34) is as follows. There must be one and only one pore in the center of each hexagonal lattice cell of a PAA, as shown in the PAA surface schematic (Fig. 5). This means that the number of pores and lattice cells is equal on a PAA. Therefore, the PAA pore density is essentially the lattice cell density of a PAA. The lattice cell density equals 1 cm^2 divided by the surface area of one hexagonal lattice cell, and this area can be calculated using D_i. D_i is the distance between two adjacent nanopore centers, as shown by the red line connecting lattice cells a and b in Fig. 5. It is equivalent to the distance between two parallel sides of a hexagonal lattice cell, as shown by the red line in lattice cell c of Fig. 5. A standard hexagonal lattice cell can be equally divided into six equilateral triangles, as shown by the six olive triangles in lattice cell d of Fig. 5. This means that the area of a lattice cell is six times the area of an equilateral triangle. As shown by the olive triangle in lattice cell e of Fig. 5, the area of an equilateral triangle is given by eqn (35):

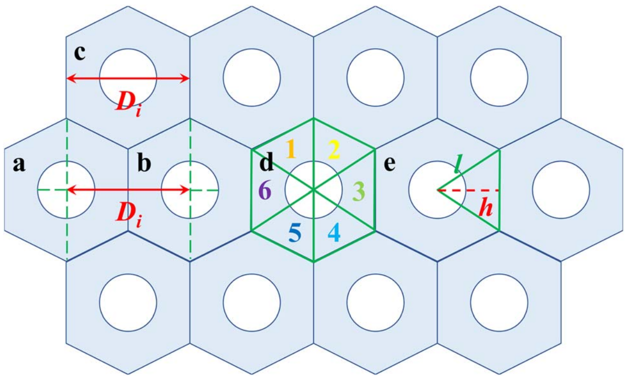

Fig. 5 Schematic of PAA surface.

$$A_\Delta = \frac{1}{2}hl = \frac{1}{2}h\left(\frac{2}{\sqrt{3}}h\right) = \frac{1}{\sqrt{3}}h^2 = \frac{1}{\sqrt{3}}\left(\frac{D_i}{2}\right)^2 = \frac{{D_i}^2}{4\sqrt{3}} \tag{35}$$

The area of a hexagonal lattice cell is given by eqn (36):

$$A_h = 6A_\Delta = \frac{\sqrt{3}{D_i}^2}{2} \tag{36}$$

According to the definition of pore density, the ρ (which is the lattice cell density, in fact) calculation formula is obtained and given by eqn (37):

$$\rho = \frac{1\ \text{cm}^2}{A_h} = \frac{10^{14}\ \text{nm}^2}{\frac{\sqrt{3}{D_i}^2}{2}\ \text{nm}^2} = \frac{2 \times 10^{14}}{\sqrt{3} \times {D_i}^2} \tag{37}$$

Going a step further, since D_i is the function of U as shown in formulas (1) and (6), formula (37) can be further derived as two new ρ calculation formulas with U as the independent variable by substituting formulas (1) and (6) into it. After substituting the optimal universal D_i calculation formula (1) into formula (37), the universal ρ calculation formula is obtained, as shown in eqn (38):

$$\rho = \frac{1.85 \times 10^{13}}{U^2} \quad \langle \text{universal} \rangle \tag{38}$$

After substituting the D_i calculation formula (6) specific to sulfuric acid anodization into formula (37), the ρ calculation formula specific to sulfuric acid anodization is obtained, as shown in eqn (39):

$$\rho = \frac{1.15 \times 10^{14}}{(1.99U + 12.1)^2} \quad \langle \text{sulfuric} \rangle \tag{39}$$

Based on further derivation, eqn (38) is also the optimal calculation formula for oxalic, phosphoric, inorganic, and organic acid anodization.

Section summary: According to a series of derivations, the existing optimal ρ calculation formulas with U as the independent variable are shown as follows:

$$\rho = \frac{1.85 \times 10^{13}}{U^2} \quad \langle \text{universal} \rangle \tag{38}$$

$$\rho = \frac{1.85 \times 10^{13}}{U^2} \quad \langle \text{oxalic} \rangle \tag{38}$$

$$\rho = \frac{1.15 \times 10^{14}}{(1.99U + 12.1)^2} \quad \langle \text{sulfuric} \rangle \tag{39}$$

$$\rho = \frac{1.85 \times 10^{13}}{U^2} \quad \langle \text{phosphoric} \rangle \tag{38}$$

$$\rho = \frac{1.85 \times 10^{13}}{U^2} \quad \langle \text{inorganic} \rangle \tag{38}$$

$$\rho = \frac{1.85 \times 10^{13}}{U^2} \quad \langle \text{organic} \rangle \tag{38}$$

Eqn (38) is the optimal ρ calculation formula in almost all cases. The only exception is for sulfuric acid anodization, where formula (39) offers a slight advantage over formula (38).

9 Porosity (σ)

σ is the eighth PAA structural parameter, which is also a second artificially defined parameter. It is defined as the ratio of the total surface area occupied by all pores to the total surface area of a PAA. It is a derived structural parameter, which is calculated from D_i and D_p. For a well-ordered PAA with a closely packed hexagonally arranged lattice of pores without widening hole treatment, σ can be calculated by formula (40)::[27,61,64,65]

$$\sigma = \frac{\pi}{2\sqrt{3}} \times \left(\frac{D_p}{D_i}\right)^2 \approx 0.907 \times \left(\frac{D_p}{D_i}\right)^2 \tag{40}$$

where σ is the porosity and a dimensionless parameter, D_i is the interpore distance in units of nm, and D_p is the pore diameter in units of nm.

The derivation process of eqn (40) is as follows. There must be one and only one pore in the center of each hexagonal lattice cell of a PAA, as shown in the PAA surface schematic of Fig. 5. This means that for a perfect well-ordered PAA, σ can be calculated using the circular pore area and the hexagonal lattice area from the same single lattice cell. It equals the ratio of the circular pore area to the hexagonal lattice area. The circular pore area (A_c) can be calculated using eqn (41):

$$A_c = \pi\left(\frac{D_p}{2}\right)^2 = \frac{\pi}{4}(D_p)^2 \tag{41}$$

The hexagonal lattice area (A_h) has already been given by eqn (36) in the previous discussion. Thus, the formula (40) can be derived from A_c/A_h, as shown in the calculation process in eqn (42):

$$\sigma = \frac{A_c}{A_h} = \frac{\frac{\pi}{4}(D_p)^2}{\frac{\sqrt{3}}{2}(D_i)^2} = \frac{\pi}{2\sqrt{3}} \times \left(\frac{D_p}{D_i}\right)^2 \approx 0.907 \times \left(\frac{D_p}{D_i}\right)^2 \tag{42}$$

Going a step further, since both D_i and D_p are a function of U, as shown in formulas (1), (6), (9), (11) and (12), formula (40) can be further derived into simplified σ calculation formulas with U as the only independent variable. After substituting the universal D_i calculation formula (1) and universal D_p calculation formula (11) into formula (40), the universal σ calculation formula is obtained, as shown in eqn (43):

$$\sigma = \frac{(0.709U + 4.986)^2}{6.891U^2} \quad \langle \text{universal} \rangle \tag{43}$$

After substituting the oxalic D_i calculation formula (1) and oxalic D_p calculation formula (9) into (40), the oxalic σ calculation formula is obtained as a constant equal to 11.75%, as shown in eqn (44):

$$\sigma = 11.75\% \, \langle \text{oxalic} \rangle \tag{44}$$

This result is similar to the 10% porosity rule for PAA.[98] After substituting the sulfuric D_i calculation formula (6) and sulfuric D_p calculation formula (12) into formula (40), the σ calculation formula specific to sulfuric acid anodization is obtained, as shown in eqn (45):

$$\sigma = \frac{177.8\ e^{0.04U}}{(1.99U + 12.1)^2} \quad \langle \text{sulfuric} \rangle \tag{45}$$

Moreover, based on further derivation, eqn (43) is the optimal calculation for phosphoric acid anodization.

Notably, both σ and ρ (discussed in the previous section) are artificially defined structural parameters of PAA, rather than natural ones. They cannot be directly measured experimentally, but must be derived through calculations based on other structural parameters. Despite many references concerning σ and ρ, all reported values for σ and ρ are calculated from D_i and D_p, and are not measured experimentally.[27,61,64,65,98] In scientific research, the accuracy of a theoretical model or formula needs to be determined through experimental verification, specifically by examining how well its calculated outcomes fit the measured data. Without experimentally measured σ and ρ data for practical validation, assessing the consistency and accuracy of their formulas is inherently meaningless, whether or not other structural parameters like D_i and D_p are used for cross-reference. The key to resolving the issue of consistency and accuracy assessment for the σ and ρ formula lies in whether a new measuring technique can be developed to effectively measure the experimental data of σ and ρ in the future. Given the current lack of experimental measurement data for σ and ρ, their existing calculation formulas can only be regarded as the correct results of logical theoretical derivation. The development of an experimental measurement technique for σ and ρ remains a significant research gap at present and a meaningful research topic for future work.

Section summary: according to a series of derivations, the existing optimal σ calculation formulas with U as the only independent variable are shown as follows:

$$\sigma = \frac{(0.709U + 4.986)^2}{6.891U^2} \quad \langle \text{universal} \rangle \tag{43}$$

$$\sigma = 11.75\% \, \langle \text{oxalic} \rangle \tag{44}$$

$$\sigma = \frac{177.8\ e^{0.04U}}{(1.99U + 12.1)^2} \quad \langle \text{sulfuric} \rangle \tag{45}$$

$$\sigma = \frac{(0.709U + 4.986)^2}{6.891U^2} \quad \langle \text{phosphoric} \rangle \tag{43}$$

Eqn (43) is the universal σ calculation formula for common cases. The first exception is for oxalic acid as the electrolyte, where formula (44) is slightly better than formula (43). The second exception is for sulfuric acid as the electrolyte, where formula (45) is slightly better than formula (43).

$$
\begin{cases}
\text{Interpore distance}\begin{cases}
D_{\mathrm{i}} = 2.5U \\
D_{\mathrm{i}} = 2.77U \\
D_{\mathrm{i}} = 2.8U \\
D_{\mathrm{i}} = 2.75U - 5.2 \quad \langle \mathrm{H_2C_2O_4} \rangle \\
D_i = \begin{cases} 2.00U + 14.5 \quad (U \leq 20\ \mathrm{V}) \\ 2.81U - 1.70 \quad (U \geq 20\ \mathrm{V}) \end{cases} \langle \mathrm{H_2C_2O_4} \rangle \\
D_{\mathrm{i}} = 1.99U + 12.1 \quad \langle \mathrm{H_2SO_4} \rangle
\end{cases} \\
\text{Pore diameter}\begin{cases}
D_{\mathrm{p}} = 0.9U \\
D_{\mathrm{p}} = 1.29U \\
D_{\mathrm{p}} = 0.709U + 4.986 \\
D_{\mathrm{p}} = 14\,\mathrm{e}^{0.02U}
\end{cases} \\
\text{Pore wall thickness}\left\{ T_{\mathrm{w}} = \dfrac{D_{\mathrm{i}} - D_{\mathrm{p}}}{2} \right. \\
\text{Barrier layer thickness}\begin{cases}
T_{\mathrm{b}} = U \\
T_{\mathrm{b}} = 1.05U \\
T_{\mathrm{b}} = 1.1U \\
T_{\mathrm{b}} = 1.14U \\
T_{\mathrm{b}} = 1.3U \\
T_{\mathrm{b}} = 1.4U \\
T_{\mathrm{b}} = 1.12T_{\mathrm{w}} \quad \langle \mathrm{H_2C_2O_4} \rangle \\
T_{\mathrm{b}} = 1.33T_{\mathrm{w}} \quad \langle \mathrm{H_2SO_4} \rangle \\
T_{\mathrm{b}} \cong \dfrac{D_{\mathrm{i}}}{2}
\end{cases} \\
\text{Porous layer thickness}\left\{ T_{\mathrm{p}} = L_{\mathrm{p}} = 125.53D - 147.75 \right. \\
\text{Oxide layer thickness}\left\{ T_{\mathrm{o}} = T_{\mathrm{b}} + T_{\mathrm{p}} \right. \\
\text{Pore density}\left\{ \rho = \dfrac{2 \times 10^{14}}{\sqrt{3}{D_{\mathrm{i}}}^2} \right. \\
\text{Porosity}\left\{ \sigma = \dfrac{\pi}{2\sqrt{3}}\left(\dfrac{D_{\mathrm{p}}}{D_{\mathrm{i}}}\right)^2 \right.
\end{cases}
$$

10 Summary and outlook

There are eight key structural parameters for PAA in total: interpore distance (D_{i}), pore diameter (D_{p}), pore wall thickness (T_{w}), barrier layer thickness (T_{b}), porous layer thickness (T_{p}) also known as pore channel length (L_{p}), oxide layer thickness (T_{o}), pore density (ρ) and porosity (σ), respectively. In current published research studies, the most common calculation formulas of the eight key PAA structural parameters are summarized and organized as follows:

According to a series of competitive screening for the most common calculation formulas of the eight PAA structural parameters, the optimal formulas of each structural parameter for various electrolyte systems are confirmed. After further using U to unify the independent variables of the existing optimal formulas, the universal equation set for the PAA structural parameter calculation with U as the unified independent variable is formulated as follows:

$$
\text{Universal PAA equation set}\begin{cases}
D_{\mathrm{i}} = 2.5U \\
D_{\mathrm{p}} = 0.709U + 4.986 \\
T_{\mathrm{w}} = 0.896U - 2.493 \\
T_{\mathrm{b}} = 1.1U \\
T_{\mathrm{p}} = L_{\mathrm{p}} = 125.53D - 147.75 \\
T_{\mathrm{o}} = 1.1U + 125.53D - 147.75 \\
\rho = \dfrac{1.85 \times 10^{13}}{U^2} \\
\sigma = \dfrac{(0.709U + 4.986)^2}{6.891U^2}
\end{cases}
$$

where U is the anodization voltage with units of V, and D is the anodization duration in units of min. The universal PAA equation set demonstrates high accuracies across most situations. It is a reliable equation set that can be widely used for all PAA structural parameter calculations.

The specialized equation set for the PAA structural parameter calculation with U as the unified independent variable is formulated as follows:

where U is the anodization voltage in units of V, and D is the anodization duration in units of min. The specialized equation set for the PAA structural parameter calculation will provide more accurate calculation results, if the anodization of a PAA is specified in a specific electrolyte.

The proposal of an equation set for the PAA structural parameter calculation confirms the existing optimal PAA structural parameter calculation formulas for mild anodization. It provides a systematic and accurate theoretical model and mathematical tool for designing and calculating PAA structures, according to practical requirements in scientific research and engineering applications.

It should be emphasized that this review provides a systematic summary and competitive screening of the most widely adopted existing formulas for calculating PAA structural parameters. The formulas screened here represent those regarded as the most universal and accurate up to now.

$$\text{Specialized PAA equation set}\left\{\begin{array}{l}
D_{\mathrm{i}}\left\{\begin{array}{ll}
D_i = 2.5U & \langle\text{oxalic}\rangle \\
D_{\mathrm{i}} = 1.99U + 12.1 & \langle\text{sulfuric}\rangle \\
D_{\mathrm{i}} = 2.5U & \langle\text{phosphoric}\rangle \\
D_{\mathrm{i}} = 2.5U & \langle\text{inorganic}\rangle \\
D_{\mathrm{i}} = 2.5U & \langle\text{organic}\rangle
\end{array}\right. \\
D_{\mathrm{p}}\left\{\begin{array}{ll}
D_{\mathrm{p}} = 0.9U & \langle\text{oxalic}\rangle \\
D_{\mathrm{p}} = 14\,\mathrm{e}^{0.02U} & \langle\text{sulfuric}\rangle \\
D_{\mathrm{p}} = 0.709U + 4.986 & \langle\text{phosphoric}\rangle
\end{array}\right. \\
T_{\mathrm{w}}\left\{\begin{array}{ll}
T_{\mathrm{w}} = 0.8U & \langle\text{oxalic}\rangle \\
T_{\mathrm{w}} = 0.995U - 7\,\mathrm{e}^{0.02U} + 6.05 & \langle\text{sulfuric}\rangle \\
T_{\mathrm{w}} = 0.896U - 2.493 & \langle\text{phosphoric}\rangle
\end{array}\right. \\
T_{\mathrm{b}}\left\{\begin{array}{ll}
T_{\mathrm{b}} = 1.1U & \langle\text{oxalic}\rangle \\
T_{\mathrm{b}} = 1.1U & \langle\text{sulfuric}\rangle \\
T_{\mathrm{b}} = 1.14U & \langle\text{phosphoric}\rangle
\end{array}\right. \\
L_{\mathrm{p}}\ \left\{ L_{\mathrm{p}} = T_{\mathrm{p}} = 125.53D - 147.75\right. \\
T_{\mathrm{o}}\left\{\begin{array}{ll}
T_{\mathrm{o}} = 1.1U + 125.53D - 147.75 & \langle\text{oxalic}\rangle \\
T_{\mathrm{o}} = 1.1U + 125.53D - 147.75 & \langle\text{sulfuric}\rangle \\
T_{\mathrm{o}} = 1.14U + 125.53D - 147.75 & \langle\text{phosphoric}\rangle
\end{array}\right. \\
\rho\left\{\begin{array}{ll}
\rho = \dfrac{1.85\times10^{13}}{U^2} & \langle\text{oxalic}\rangle \\
\rho = \dfrac{1.15\times10^{14}}{(1.99U + 12.1)^2} & \langle\text{sulfuric}\rangle \\
\rho = \dfrac{1.85\times10^{13}}{U^2} & \langle\text{phosphoric}\rangle \\
\rho = \dfrac{1.85\times10^{13}}{U^2} & \langle\text{inorganic}\rangle \\
\rho = \dfrac{1.85\times10^{13}}{U^2} & \langle\text{organic}\rangle
\end{array}\right. \\
\sigma\left\{\begin{array}{ll}
\sigma = 11.75\% & \langle\text{oxalic}\rangle \\
\sigma = \dfrac{177.8e^{0.04U}}{(1.99U + 12.1)^2} & \langle\text{sulfuric}\rangle \\
\sigma = \dfrac{(0.709U + 4.986)^2}{6.891U^2} & \langle\text{phosphoric}\rangle
\end{array}\right.
\end{array}\right.$$

However, this does not imply that they are absolutely universal or accurate in an objective sense. Significant potential remains for improving the universality and accuracy of the existing formulas, as clearly demonstrated by the MSE statistics for the D_i, D_p, and T_b calculation formulas in Tables 1–3, respectively. The most critical problem of the existing mainstream PAA structural parameter calculation formulas is that these existing mainstream formulas are primarily expressed as single-variable functions of U, but that voltage is not the sole factor influencing the PAA structural parameters. Besides voltage, many other conditions such as the anodization temperature, electrolyte concentration, electrolyte type and anodization duration also influence various PAA structural parameters to different extents.[59,83,108] For example, the anodization temperature is almost the second most significant factor influencing the PAA structural parameters, after voltage. The structural parameters affected by temperature include D_p, T_w, T_b, T_p, T_o and σ. While the impact of temperature on the PAA structural parameters has been qualitatively mentioned in numerous studies, it is unsatisfactory that systematic quantitative investigations dedicated to temperature effects, particularly those regarding local temperature, are scarcely reported. Existing calculation formulas for PAA structural parameters neither incorporate temperature as a variable nor specify their applicable temperature ranges, which constitutes a serious limitation in the existing proposed formulas. Therefore, besides the anodization voltage, the systematic and quantitative investigation of other key anodization conditions (such as the anodization temperature, electrolyte concentration, electrolyte type, and anodization duration) that influence the structural parameters of PAA remains a significant research gap at present and a meaningful research topic for future work.

The second point to emphasize is that all calculation formulas mentioned in this review are suitable for PAA prepared by mild anodization. However, it is important to note that hard anodization is another important method for fabricating PAA,[108–110] and these formulas are not wholly suitable for the resulting PAA of hard anodization. A detailed discussion of the formulas applicable to hard-anodized PAA will be presented in our next forthcoming topical review.

Data availability

No primary research results, software or code have been included, and no new data were generated or analysed as part of this review.

Supplementary information (SI) is available. See DOI: https://doi.org/10.1039/d5ra09220e.

Conflicts of interest

The authors have no conflicts of interest to declare.

Acknowledgements

The authors acknowledge the support of the Applied Basic Research Fund of the School of Physics and Optoelectronic Engineering of Beijing University of Technology (056000513103) and the Open Project Fund of Multi-Scale Laser Forming Manufacturing Technology (056000514125528).

References

1 X. Yin, H. Zhou, M. Zhang, J. Su, X. Wang, S. Li, Z. Yang, Z. Kang and R. Zhou, C_3N nanodots inhibits Aβ peptides aggregation pathogenic path in Alzheimer's disease, *Nat. Commun.*, 2023, **14**, 5718.

2 Y. Kimura, Y. Cui, T. Suzuki, Y. Tanaka, T. Tanaka, Y. Toku and J. Yang, Growth of metal nanowire forests controlled through stress fields induced by grain gradients, *Science*, 2024, **385**, 641–646.

3 D. Moon, W. Lee, C. Lim, J. Kim, Y. Jung, H.-Y. Choi, W. S. Choi, H. Kim, Ji-H. Baek, C. Kim, J. Joo, H.-G. Oh, H. Jang, K. Watanabe, T. Taniguchi, S. Bae, J. Son, H. Ryu, J. Kwon, H. Cheong, J. W. Han, H. Jang and G.-H. Lee, Hypotaxy of wafer-scale single-crystal transition metal dichalcogenides, *Nature*, 2025, **638**, 957–964.

4 H. Hilal, Q. Zhao, J. Kim, S. Lee, H. MohammadNavid, S. Yoo, S. Lee, W. Park, W. Park, J. Lee, W. L. Joong, I. Jung and S. Park, Three-dimensional nanoframes with dual rims as nanoprobes for biosensing, *Nat. Commun.*, 2022, **13**, 4813.

5 J. Tao, R. Gao, G. Lin, C. Chu, Y. Sun, C. Yu, Y. Ma and H. Qiu, Synthesis of noble metal nanoarrays via agglomeration and metallurgy for acidic water electrolysis, *Nat. Commun.*, 2025, **16**, 4996.

6 S. Zhao, W. Peng, L. Zhou, D. Shuqi, W. Ren, E. Xu, Y. Xiao, M. Zhang, M. Huang, Y. Shen and C.-W. Nan, Metal-organic cage crosslinked nanocomposites with enhanced high-temperature capacitive energy storage performance, *Nat. Commun.*, 2025, **16**, 769.

7 A. O. Denisov, V. Reckova, S. Cances, M. J. Ruckriegel, M. Masseroni, C. Adam, C. Tong, J. D. Gerber, W. W. Huang, K. Watanabe, T. Taniguchi, T. Ihn, K. Ensslin and H. Duprez, Spin-valley protected Kramers pair in bilayer graphene, *Nat. Nanotechnol.*, 2025, **20**, 494–499.

8 H. Luo, J. Lv, P. Wen, S. Zhang, M. Wen and Z. Yang, Supramolecular polyrotaxane-based nano-theranostics enable cancer-cell stiffening for enhanced T-cell-mediated anticancer immunotherapy, *Nat. Commun.*, 2025, **16**, 2331.

9 X. Wang, Z. Yuan, L. Tingting, K. Wang, W. Dong, M. Lu, Y. Zhang, Z. Wu, A. Tang and X. Bai, Sequential addition of cations increases photoluminescence quantum yield of metal nanoclusters near unity, *Nat. Commun.*, 2025, **16**, 587.

10 S. C. Jin, S. Park, N.-U. K. Seo, Y.-C. Kang, C.-W. Lee and H. Y. Jung, Zincophilic CuO as electron sponge to facilitate dendrite-free zinc-based flow battery, *Nat. Commun.*, 2025, **16**, 844.

11 X. He, H. Gu, Y. Ma, Y. Cai, H. Jiang, Y. Zhang, H. Xie, M. Yang, X. Fan, L. Guo, Z. Yang and C. Hu, Light patterning semiconductor nanoparticles by modulating surface charges, *Nat. Commun.*, 2024, **15**, 9843.

12 G. Wang, T. Dvir, G. P. Mazur, C.-X. Liu, N. van Loo, S. L. D. Ten Haaf, A. Bordin, S. Gazibegovic, G. Badawy, E. P. A. M. Bakkers, M. Wimmer and L. P. Kouwenhoven, Singlet and triplet Cooper pair splitting in hybrid superconducting nanowires, *Nature*, 2022, **612**, 448–453.

13 Y. Liu, M. Li, K. Jiang, Y. Zhang, P. Gong, S. Song, L. Dong, H. Liang, X. Huang, J. Wang, W. Li and C.-W. Nan, Radiation-hardened dendritic-like nanocomposite films with ultrahigh capacitive energy density, *Nat. Commun.*, 2025, **16**, 3882.

14 B. Lyu, J. Chen, S. Wang, S. Lou, P. Shen, J. Xie, L. Qiu, I. Mitchell, C. Li, C. Hu, X. Zhou, K. Watanabe, T. Taniguchi, X. Wang, J. Jia, L. Qi, G. Chen, T. Li, S. Wang, W. Ouyang, O. Hod, F. Ding, M. Urbakh and Z. Shi, Graphene nanoribbons grown in hBN stacks for high-performance electronics, *Nature*, 2024, **628**, 758–764.

15 Z. Miao, W. Jiang, H. Qiao, W. Xunbin, Y.-W. Zhong, R. Hao and M. Gu, A 3D nanoscale optical disk memory with petabit capacity, *Nature*, 2024, **626**, 772–778.

16 S. Lee, R. D. Kibler, G. Ahn, Y. Hsia, A. J. Borst, A. Philomin, M. A. Kennedy, B. Huang, B. Stoddard and D. Baker, Four-component protein nanocages designed by programmed symmetry breaking, *Nature*, 2025, **638**, 546–552.

17 W. Peng, W. Tai, B. Li, H. Wang, T. Wang, S. Guo, X. Zhang, P. Dong, C. Tian, S. Feng, L. Yang, C. Gong and B. Zheng, Inhalable nanocatalytic therapeutics for viral pneumonia, *Nat. Mater.*, 2025, **24**, 637–648.

18 Y. Song, N. Xu, G. Liu, H. Qi, W. Zhao, B. Zhu, Z. Lin and Z. Jia, High-yield solar-driven atmospheric water harvesting of metal-organic-framework-derived nanoporous carbon with fast-diffusion water channels, *Nat. Nanotechnol.*, 2022, **17**, 857–863.

19 S. Panda, T. Maity, S. Sarkar, A. K. Manna, J. Mondal and R. Haldar, Diffusion-programmed catalysis in nanoporous material, *Nat. Commun.*, 2025, **16**, 1231.

20 D. Wang, N. B. Saleh, A. Byro, R. Zepp, E. Sahle-Demessie, T. P. Luxton, K. T. Ho, R. M. Burgess, M. Flury, J. C. White and C. Su, Nano-enabled pesticides for sustainable agriculture and global food security, *Nat. Nanotechnol.*, 2022, **17**, 347–360.

21 L. Wei, J. Liu and G. Jiang, Nanoparticle-specific transformations dictate nanoparticle effects associated with plants and implications for nanotechnology use in agriculture, *Nat. Commun.*, 2024, **15**, 7389.

22 H. Peng, B. Cai, Y. Zhang, L. Gao, Z. Pei-Yan, L. Zhou, S. Zhang, W. Liang, Q.-F. Xuan, M. C. Koo, C.-M. Liang, L. Wen-Peng, Z.-L. Hou, T. Zhou and G.-S. Wang, Rada-terahertz-infrared compatible stealth coaxial silver nanowire@carbon nano-cable aerogel, *Angew. Chem., Int. Ed.*, 2025, **64**, e202421090.

23 V. S. Abhay Anand, M. K. Sahoo, F. Mujeeb, A. Varghese, S. Dhar, S. Lodha and A. Kumar, Novel nano-electroplating-based plasmonic platform for giant emission enhancement in monolayer semiconductors, *ACS Appl. Mater. Interfaces*, 2023, **15**, 57783–57790.

24 C. Xue, J. Zhao, Y. Wu, H. Yu, S. Yang, L. Wang, W. Zhao, Q. Wu, Z. Zhu, B. Liu, X. Zhang, W. Zhou and R. Tai, Fabrication of Larger-area high-aspect-ratio periodic nanostructures on various substrates by soft X-ray interference lithography, *Appl. Surf. Sci.*, 2017, **425**, 553–557.

25 B. X. E. Desbiolles, E. de Coulon, A. Bertsch, S. Rohr and P. Renaud, Intracellular recording of cardiomyocyte action potentials with nanopatterned volcano-shaped microelectrode arrays, *Nano Lett.*, 2019, **19**, 6173–6181.

26 J. S. Wojciech and Z. Bojar, Synthesis of anodic aluminum oxide (AAO) at relatively high temperatures. Study of the influence of anodization conditions on the alumina structural features, *Surf. Coat. Technol.*, 2011, 265–272.

27 I. Vida-Simiti, D. Nemes, N. Jumate, G. Thalmaier and N. Sechel, Self-ordered nanoporous alumina templates formed by anodization of aluminum in oxalic acid, *JOM*, 2012, **64**, 1143–1147.

28 A. K. Eessaa and A. M. El-Shamy, Review on fabrication, characterization, and applications of porous anodic aluminum oxide films with tunable pore sizes for emerging technologies, *Microelectron. Eng.*, 2023, **279**, 112061.

29 B. Lee, M. Kang, K. Lee, Y. Chae, K.-J. Yoon, D.-S. Lee and I. Park, Multigas identification by temperature-modulated operation of a single anodic aluminum oxide gas sensor platform and deep learning algorithm, *ACS Sens.*, 2025, **10**, 954–964.

30 C.-C. Lee, C.-W. Chen, J.-S. Lin, S. H. Wang, C.-S. Lee, C.-C. Chen, Y.-H. Lin and C.-Y. Chen, Effect of anodization treatment on the thickness, hardness, and microstructural characterization of anodic aluminum oxide film on AA6061 and critical patent analysis, *J. Mater. Eng. Perform.*, 2022, **31**, 667–681.

31 G. R. Kramer, F. A. Bruera, P. D. Zapata and A. E. Ares, Aluminum oxide coatings as nanoadsorbents for the treatment of effluents colored with Eriochrome black T, *Coating*, 2025, **15**, 15040488.

32 A. Wang, Y. Hang, J. Wang, W. Tan and N. Wu, Machine learning-assisted light management and electromagnetic field modulation of large-area plasmonic coaxial cylindrical pillar/ring nanoarray patterns, *J. Phys. Chem. C*, 2024, **128**, 12495–12502.

33 S. L. Lee, J. Thomas, C.-Y. Mou, C.-L. Liu and K.-L. Tung, High-performance separation for ultra-low concentration nanoparticles with mesoporous silica thin membrane, *Sep. Purif. Technol.*, 2024, **350**, 127918.

34 C.-C. Fan, Y.-H. Liu and C.-J. Lu, Separation of C1 – C15 alkanes with a disk-shaped aluminum column employing mesoporous AAO as the stationary phase, *Anal. Chem.*, 2022, **94**, 15570–15577.

35 A. Anil Chandra, Z. Huang, B. Amit, W. Van Geertruyden, D. Gao and M. Wojciech, Evaluation of Nano-porous alumina membranes for hemodialysis application, *ASAIO J.*, 2009, **55**, 217–223.

36 M. Makela and Z. L. P. T. Lin, Surface functionalized anodic aluminum oxide membrane for opto-nanofluidic SARS-CoV-A genomic target detection, *IEEE Sens. J.*, 2021, **21**, 22645–22650.

37 Z. Zhang, M. Brady, B. K. Amarsingh, J.-R. Park, E. R. Jong and D. Choi, Electrochemical Characterization of $LiMn_2O_4$ nanowires fabricated by sol-gel for lithium-ion rechargeable batteries, *Mater. Lett.*, 2020, **273**, 127923.

38 Y. Li, L. Feng, J. Zhu, H. Zhang, S. Ha and K. Zhang, Structural and optical properties of Ga_2O_3 nanorod arrays sputtered using AAO templates, *Mater. Lett.*, 2025, **392**, 138569.

39 K. Roman, M. L. Smith, N. C. A. Seaton, M. L. Odlyzko, O. Masiuchok, R. Jeanne, P. B. Amama and B. J. H. Stadler, Sustainable manufacturing of vertical carbon nanotube (CNT) arrays inside insulating nanoporous membranes using nickel magnetic nanowires (MNWs), *ACS Appl. Nano Mater.*, 2024, **7**, 24866–24874.

40 G. Chen, F. Han, H. Ma, L. Pei, Z. Zhou, P. Wang, X. Li, G. Meng and B. Wei, High density 3D carbon tube nanoarray electrode boosting the capacitance of filter capacitor, *Nano-Micro Lett.*, 2024, **16**, 235.

41 Z. Lin, G.-L. Yang, W.-J. Ding, Y.-Q. Cao, W.-M. Li and Ai-D. Li, Growth behavior of Ir metal formed by atomic layer deposition in the nanopores of anodic aluminum oxide, *Dalton Trans.*, 2022, **51**, 9664.

42 J. Shen, Z. Hu, L. Quigley and H. Wang, Controlled growth of vertically aligned nanocomposites through an Au seeding-assisted method, *ACS Omega*, 2023, **8**, 37140–37146.

43 J. Chen, Z. He and Y. Wang, AAO-ZnO nanocomposite coatings on aluminum alloy surface with high bonding strength and long-lasting antibacterial properties, *Chem. Eng. J.*, 2024, **497**, 154414.

44 B. A. Tran, M. T. Nguyen, T. Quang Le, T. C.-T. Pham, T.-P. T. Pham, T. L. Anh and H.-D. Nguyen, High-performance red-emitting InGaN/AlGaN nanowire light-emitting Diodes grown through porous template, *Mater. Sci. Semicond. Process.*, 2024, **169**, 107894.

45 D. Xu, Z. Congmian and Z. Hao, Morphology and growth mechanism of amorphous silicon carbide sputtered on anodic aluminum template by radio frequency magnetron sputtering, *Ceram. Int.*, 2020, **46**, 19629–19633.

46 H. Masuda and K. Fukuda, Ordered metal nanohole arrays made by a two-step replication of honeycomb structures of anodic alumina, *Science*, 1995, **268**, 1466–1468.

47 I. V. Roslyakov, E. O. Sotnichuk, S. V. Sotnichuk, S. E. Kushnir and K. S. Napolskii, Kinetic and crystallographic control of self-ordering of pores in anodic aluminium oxide, *J. Solid State Electrochem.*, 2025, **29**, 1341–1373.

48 B. Tazneva, I. Vrublevshy, V. Videkow and N. Luspha, Role of electrode temperature in anodic growth of sulfuric acid alumina films, *J. Solid State Electrochem.*, 2025, **29**, 1459–1465.

49 Z. Song, X. Zhang, Y. Yang, P. Hou, J. Chen and S. Liang, Preparation and field emission properties of Ni nanowire arrays with different length-diameter ratios, *J. Alloys Compd.*, 2025, **1010**, 178203.

50 J. Dai, J. Singh and N. Yamamoto, Nonbrittle nanopore deformation of anodic aluminum oxide membranes, *J. Am. Ceram. Soc.*, 2018, **101**, 2170–2180.

51 G.-O. Ana, R. Jerome and A. Laurent, Nanocontrolled thinning of the barrier layer thickness of porous anodic films using galvanodynamic polarization of aluminum alloys, *Electrochim. Acta*, 2024, **479**, 143894.

52 G. Arulkumar, P. Swaminathan and L. Neelakantan, Anodic aluminum oxide template assisted synthesis of copper nanowires using a galvanic displacement process for electrochemical denitrification, *ACS Appl. Nano Mater.*, 2019, **2**, 5981–5988.

53 A. Adugna Ayalew, X. Han and M. Sakairi, Effect of Substrate temperature and electrolyte composition on the fabrication of through-hole porous AAO membrane with SF-MDC, *Mater. Chem. Phys.*, 2024, **323**, 129658.

54 B. A. Tran, M. T. Nguyen, T. Quang Le, T. Cao-Thanh Pham, T.-P. T. Pham, T. L. Anh and H.-D. Nguyen, High-performance red-emitting InGaN/AlGaN nanowire light-emitting diodes grown through porous template, *Mater. Sci. Semicond. Process.*, 2024, **169**, 107894.

55 A. M. Abd-Elnaiem, Z. A. Mohamed, S. El. Soliman and A. Mohamed, Synthesis, characterization, and optical sensing of hydrophilic anodic alumina films, *Opt. Mater.*, 2024, **157**, 116390.

56 Z. Leszek, G. D. Sulka, J. Szeremeta and M. Jaskula, Porous anodic alumina formed by anodization of aluminum alloy (AAO1050) and high purity aluminum, *Electrochim. Acta*, 2010, **55**, 4377–4386.

57 J. De Laet, H. Terryn and J. Vereecken, Development of an optical model for steady state porous anodic films on aluminium formed in phosphoric acid, *Thin Solid Films*, 1998, **320**, 241–252.

58 H. d. L. Lira and R. Paterson, New and modified anodic alumina membranes Part III. Preparation and characterization by gas diffusion of 5 nm pore size anodic alumina membranes, *J. Membr. Sci.*, 2002, **206**, 375–387.

59 S.-K. Hwang, S.-H. Jeong, H.-Y. Hwang, O.-J. Lee and K.-H. Lee, Fabrication of highly ordered pore array in anodic aluminum oxide, *Korean J. Chem. Eng.*, 2002, **19**, 467473.

60 K. Ebihara, H. Takahashi and M. Nagayama, Structure and density of anodic oxide films formed on aluminum in oxalic acid solutions, *J. Met. Finish. Soc. Jpn.*, 1983, **34**, 548–553.

61 K. Ebihara, H. Takahashi and M. Nagayama, Structure and density of anodic oxide films formed on aluminum in sulfuric acid solutions, *J. Met. Finish. Soc. Jpn.*, 1982, **33**, 156–164.

62 P. Ramana Reddy, K. M. Ajith and N. K. Udayashankar, Morphology and photoluminescence of nano-porous anodic alumina membranes obtained in oxalic acid at different anodization potentials, *Nano Express*, 2020, **1**, 010047.

63 L. Zaraska, W. J. Stepniowski, E. Ciepiela and G. D. Sulka, The effect of anodizing temperature on structural features and hexagonal arrangement of nanopores in alumina

synthesized by two-step anodizing in oxalic acid, *Thin Solid Films*, 2013, **534**, 155–161.

64 L. Zaraska, G. D. Sulka and M. Jaskula, Anodic alumina membranes with defined pore diameters and thicknesses obtained by adjusting the anodizing duration and pore opening/widening time, *J. Solid State Electrochem.*, 2011, **15**, 2427–2436.

65 C. V. Manzano, D. Ramos, L. Pethö, G. Bürki, J. Michler and L. Philippe, Controlling the color and effective refractive index of metal-anodic aluminum oxide (AAO)-Al nanostructures: Morphology of AAO, *J. Phys. Chem. C*, 2018, **122**, 957–963.

66 C. V. Manzano, J. P. Best, J. J. Schwiedrzik, A. Cantarero, J. Michler and L. Philoppe, The influence of thickness, interpore distance and compositional structure on the optical properties of self-ordered anodic aluminum oxide films, *J. Mater. Chem. C*, 2016, **4**, 7658.

67 J. Martín, C. V. Manzano, O. Caballero-Calero and M. Martín-González, High-aspect-ratio and highly ordered 15-nm porous alumina templates, *ACS Appl. Mater. Interfaces*, 2013, **5**, 72–79.

68 C. V. Manzano, J. Martín and M. S. Martín-González, Ultra-narrow 12 nm pore diameter self-ordered anodic alumina templates, *Microporous Mesoporous Mater.*, 2014, **184**, 177–183.

69 J. Martín, C. V. Manzano and M. Martín-González, In-depth study of self-ordered porous alumina in the 140-440 nm pore diameter range, *Microporous Mesoporous Mater.*, 2012, **151**, 311–316.

70 A. Shunta, T. Kikuchi, S. Natsui and R. O. Suzuki, Nanostructural characterization of large-scale porous alumina fabricated via anodizing in arsenic acid solution, *Appl. Surf. Sci.*, 2017, **403**, 652–661.

71 S. Ono, M. Saito and H. Asoh, Self-ordering of anodic porous alumina formed in organic acid electrolytes, *Electrochim. Acta*, 2005, **51**, 827–833.

72 S. Ono, M. Saito, M. Ishiguro and H. Asoh, Controlling factor of self-ordering of anodic porous alumina, *J. Electrochem. Soc.*, 2004, **151**, B473.

73 Y. Ahn and J. Y. Son, Formation of ferrolelctric multi-domains and electrical conduction in epitaxial $BiFeO_3$ nanodots fabricated with AAO nanotemplates, *Ceram. Int.*, 2023, **49**, 2738–2745.

74 Z. Fang, J. Dong, Y. Fan, C. Li, Q. Han, C. Zhang, L. Zhu, X. Yan, J. Qi and W. Gao, Transfer of AuNRs into AAO nanoholes via self-assembly method for ultrasensitive SERS detection, *ACS Omega*, 2025, **10**, 18764–18774.

75 S. Matsumoto, S. Tanaka, T. Nagao, T. Shimizu, S. Shingubara and T. Ito, Evaluating the anti-biofilm performance of Si and resin based nanopillars, *J. Photopolym. Sci. Technol.*, 2024, **37**, 379–384.

76 F.-G. Zhong, X.-Y. Huang, R. Barreto and S.-H. Chen, Synthetization and photocatalytic performance of high-aspect-ratio β-Bi_2O_3 nanowires via the combination of vacuum die-casting and controllable oxidation processes in liquid phase, *Ceram. Int.*, 2025, **51**, 15802–15808.

77 Z. Song, Y. Yang, P. Hou, X. Zhang, S. Liang and J. Chen, Wave aborbing properties of Ni Nanoparticle/CNT composite film fabricated by AAO/CNTs electrode, *Heliyon*, 2024, **10**, e26054.

78 A. Belwalkar, E. Grasing, W. Van Geertruyden, Z. Huang and W. Z. Misiolek, Effect of processing parameters on pore structure and thickness of anodic aluminum oxide (AAO) tubular membranes, *J. Membr. Sci.*, 2008, **319**, 192–198.

79 A. Ruiz-Clavijo, O. Caballero-Calero and M. Martín-González, Revisiting anodic alumina templates: from fabrication to applications, *Nanoscale*, 2021, **13**, 2227.

80 H. Akbarpour, M. Mohajeri and M. Akbarpour, Pore diameter of nanoporous anodic alumina: Experimental study and application of ANFIS and MLR, *Chemom. Intell. Lab. Syst.*, 2016, **153**, 82–91.

81 A. M. Abd-Elnaiem, A. M. Mebed, A. Gaber and M. A. Abdel-Rahim, Tailoring the porous nanostructure of porous anodic alumina membrane with the impurity control, *J. Alloys Compd.*, 2016, **659**, 270–278.

82 H. Azami and M. R. Omidkhah, Modeling and optimization of characterization of nanostructure anodized aluminium oxide membranes, *J. Iran. Chem. Soc.*, 2019, **16**, 985–997.

83 F. Alejandra Bruera, G. R. Kramer, M. L. Vera and A. E. Ares, Synthesis and morphological characterization of nanoporous aluminum oxide films by using a single anodization step, *Coatings*, 2019, **9**, 115.

84 W. J. Stepniowski, D. Zasada and Z. Bojar, First step of anodization influences the final nanopore arrangement in anodized alumina, *Surf. Coat. Technol.*, 2011, **206**, 1416–1422.

85 W. L. Hwang, J. K. Anthony, H.-D. Nguyen, M. Sun-il, K. Kim, H. Lim, J. Lee and R. Fabian, Enhanced ultrafast optical nonlinearity of porous anodized alumimum oxide nanostructures, *Opt. Express*, 2009, **17**, 19093–19101.

86 B. Abad, J. Maiz and M. Martin-Gonzalez, Rules to determine thermal conductivity and density of anodic aluminum oxide (AAO) membranes, *J. Phys. Chem. C*, 2016, **120**, 5361–5370.

87 C.-A. Ku, C.-C. Wu, C.-W. Hung and C.-K. Chung, Influence of normal-to-high anodizing voltage on AAO surface hardness from 1050 aluminum alloy in oxalic acid, *Micromachines*, 2024, **15**, 683.

88 C. K. Chung, D. Dhandapani, C. J. Syu, M. W. Liao, B. Y. Chu and E. H. Kuo, Role of oxalate anions on the evolution of widened pore diameter and characteristics of room-temperature anodic aluminum oxide, *J. Electrochem. Soc.*, 2017, **164**, C121–C127.

89 V. Ali, E. Dubois, L. Michot, M. Jardat, D. Lairez, S. Durand-Vidal, C. Guibert and N. Jouault, Electrical surface properties of nanoporous alumina membranes: influence of nanochannels' curvature, roughness and composition studied via electrokinetic experiments, *R. Soc. Chem.*, 2023, **25**, 28150.

90 L. González-Rovira, L. González-Souto, P. J. Astola and C. Bravo-Benítez, Francisco Javier Botana. Assessment of the corrosion resistance of self-ordered anodic aluminum

oxide (AAO) obtained in tartaric-sulfuric acid (TSA), *Surf. Coat. Technol.*, 2020, **399**, 126131.

91 D. D. Macdonald, The point defect model for the passive state, *J. Electrochem. Soc.*, 1992, **139**, 3434.

92 G. Patermarakis, J. Chandrinos and K. Masavetas, Formulation of a holistic model for the kinetics of steady state growth of porous anodic alumina films, *J. Solid State Electrochem.*, 2007, **11**, 1191–1204.

93 W. Lee and S. Park, Porous anodic aluminum oxide: anodization and templated synthesis of functional nanostructures, *Chem. Rev.*, 2014, **114**, 7487–7556.

94 S. Kjyohito, S. Suzuki, Y. Takada, K. Abe, H. Yoshida and T. Sako, Anodization of aluminum in high-pressure carbonic acid aqueous solution, *J. Chem. Eng. Jpn.*, 2006, **39**, 90–94.

95 I. Vrublevsky, V. Parkoun, V. Sokol, J. Schreckenbach and A. G. Werner, Dissolution behavior of anodic oxide films formed in sulfanic acid on aluminum, *Microchim. Acta*, 2007, **156**, 173–179.

96 C. G. Sousa, D. C. Leitão, M. P. Proença, A. Apolinário, J. G. Correia, J. Ventura and J. P. Araújo, Tunning pore filling of anodic alumina templates by accurate control of the bottom barrier layer thickness, *Nanotechnology*, 2011, **22**, 315602.

97 D. A. Brevnov, G. V. Rama Rao, G. P. López and P. B. Atanassov, Dynamics and temperature dependence of etching processes of porous and barrier aluminum oxide layers, *Electrochim. Acta*, 2004, **49**, 2487–2494.

98 K. Nielsch, J. Choi, K. Schwirn, R. B. Wehrspohn and G. Ulrich, Self-ordering regimes of porous alumina: The 10% porosity rule, *Nano Lett.*, 2002, **2**, 677–680.

99 B. Benfedda, L. Hamadou, N. Benbrahim, A. Kadri, E. Chainet and F. Charlot, Electrochemical impedance investigation of anodic alumina barrier layer, *J. Electrochem. Soc.*, 2012, **159**, C372–C381.

100 S. Ono and N. Masuko, Effect of electric field strength on cell morphology and anion incorporation of anodic porous alumina, *ECS Trans.*, 2017, **75**, 23–31.

101 X. Zhao, S.-K. Seo, U.-J. Lee and K.-H. Lee, Controlled electrochemical dissolution of anodic aluminum oxide for preparation of open-through pore structures, *J. Electrochem. Soc.*, 2007, **154**, C553–C557.

102 Y. D. Kim, S. Choi, A. Kim and W. Lee, Ionic current rectification of porous anodic aluminum oxide (AAO) with a barrier oxide layer, *ACS Nano*, 2020, **14**, 13727–13738.

103 P. L. Alexey and K. S. Napolskii, Probing barrier oxide layer of porous anodic alumina by in situ electrochemical impedance spectroscopy, *J. Electrochem. Soc.*, 2021, **168**, 071511.

104 J. Wang, C. Suwen Law, S. Gunenthiran, H. N. Q. Tran, K. N. Tran, S. Y. Lim, A. D. Abell and A. Santos, Structural engineering of the barrier oxide layer of nanoporous anodic alumina for iontronic sensing, *ACS Appl. Mater. Interfaces*, 2022, **14**, 21181–21197.

105 X. Li, Z. Liu, L. Yang, S. Zhou, Y. Qian, Y. wu, Z. Yan, Z. Zhang, T. Li, Q. Wang, C. Zhu, X.-Y. Kong and L. Wen, An ultrasensitive 2, 4, 6-trinitrophenol nanofluidic sensor inspired by olfactory sensory neurons in sniffer dogs, *Chem. Sci.*, 2024, **15**, 19504.

106 M. Chen, C. Wang, J. Tan, J. Wang and C. Wang, Cell membrane-inspired COF/AAO hybrid nanofluidic membrane with ion current rectification properties for ultrasensitive detection of *E. coli*, *Sens. Actuators, B*, 2025, **423**, 136719.

107 L. Osama, H. T. Handal, A. M. El-Sayed Sara, E. M. Elzayat and M. Mostafa, Fabrication and optimization of alumina nanoporous membranes for drug delivery applications: A comparative study, *Nanomaterials*, 2024, **14**, 1078.

108 Y. Li, M. Zheng, L. Ma and W. Shen, Fabrication of highly ordered nanoporous alumina films by stable high-field anodization, *Nanotechnology*, 2006, **17**, 5101–5105.

109 W. Lee, J. Ran, G. Ulrich and K. Nielsch, Fast fabrication of long-range ordered porous alumina membranes by hard anodization, *Nat. Mater.*, 2006, **5**, 741–747.

110 S.-Z. Chu, K. Wada, S. Inoue, M. Isogai and A. Yasumori, Fabrication of ideally ordered nanoporous alumina films and integrated alumina nanotubule arrays by high-field anodization, *Adv. Mater.*, 2005, **17**, 2115–2119.